ANALYSIS OF LIQUID POOLING DURING LATE-STAGE SOLIDIFICATION

ANALYSIS OF LIQUID POOLING DURING LATE-STAGE SOLIDIFICATION

By

RAMEEZ ASHRAF, B.ENG

A THESIS

SUBMITTED TO THE DEPARTMENT OF MATERIALS SCIENCE & ENGINEERING AND THE SCHOOL OF GRADUATE STUDIES OF MCMASTER UNIVERSITY

IN PARTIAL FULFILMENT OF THE REQUIREMENTS FOR THE DEGREE OF

MASTERS OF APPLIED SCIENCE

MASTER OF APPLIED SCIENCE (2012)   McMaster University
(Department of Materials Science& Engineering)McMaster University

TITLE: Analysis of Liquid Pooling during Late-Stage Solidification
AUTHOR: Rameez Ashraf, B.Eng
SUPERVISOR: N.Provatas
NUMBVER OF PAGES: x,

ABSTRACT

Grain structure and secondary phases play a critical role in determining the mechanical properties of industrial alloys. The spatial variation of such phases is very closely correlated to the liquid pooling established during late stage solidification and grain boundary coalescence. Obtaining a theory that correlates the evolution of length scales during grain boundary coalescence is a critical step toward the optimization of commercial alloys. This thesis highlights various phenomena that enter such a theory. They include coarsening and coalescence of dendrites, nucleation mechanisms and changes in composition of inter-dendritic liquid where second phases tend to initially form. Quantitative phase field models of solidification to simulate casting conditions and microstructure evolution are used in combination with characterization techniques to illustrate the connection between number, size, and distribution of liquid pools. Characterization techniques include spectral analysis, and clustering analysis by way of the Hoshen-Kopleman algorithm. By characterizing late-stage liquid pools, this thesis aims to be a first step towards developing a statistical scaling theory of length scale of liquid pooling.

ACKNOWLEGEMENTS

I would like to express my sincerest gratitude to my supervisor Nikolas Provatas, who allowed me the privilege of working with him and his truly wonderful research group. His mentorship has been invaluable and his work ethic is exemplary, and still continues to amaze me. My sincerest thanks and apologies also go to his research group and collaborators, who were kind enough to entertain me with many discussions. In particular, I could have not done without Nana Ofori-Opoku, David Montiel and Jeff Hoyt's valuable insight and opinions. It has been a pleasure working alongside such fine people, and I can only hope it's the same vice-versa. Many thanks are also in order for Dr. Mikko Karttunen, who provided my first clustering code. It eventually became central to the work presented in this thesis.

I have pursued this thesis and degree, as anything else in life, with my family in mind. Not a single day goes by without me thinking of their love, encouragement and eternal support. For this, among many, many things, I will always take happyness in pursuit for their right to pursue happyness.

Honorable mentions also go out to the ladies that run McMaster's Materials Science & Engineering Department who helped me with many logistical issues and chocolate, and the Starbucks at King & Millers Lane in Dundas, ON. Most of the work seen in this thesis was done in its great ambiance.

To my parents Ashraf Niaz & Nasreen Nazeer, and my brothers

Raheel & Ahsan Ashraf

CONTENTS

LIST OF FIGURES

ix

LIST OF TABLES

INTRODUCTION

Even though history prescribes important lessons, much of Materials Science is rarely conditioned in such a manner that highlights its importance through the ages. The excellent book: A History of the World in 100 Objects (by Neil MacGregor, British art historian and museum director), paints a wonderful picture of history of humanity as a history of invention and innovation. This is exemplified in key objects that allow readers to understand the world's current state of affairs.

By extension of Neil MacGregor's argument, it is very appropriate to state that these 100 key objects existed in their useful state *only* because of the right materials. It is then only appropriate to state that materials make history. The importance of use of materials in shaping human history is such that periods of history have been labeled with materials: Stone, Bronze and the Iron Ages. The author finds that the importance of materials in culture and philosophy, and by extension art and science, is frequently understated.

If the Earth is imagined as a fiery ball at its inception 4 billion years ago, then all/most material that exists today came into being through a phase transformation from liquid to solid. This process is now known as *Solidification*. Nowhere is the process as prominent as it is in metal forming.

The need for more innovative alloys has allowed for solidification to evolve into a science, and phenomena that characterize it have been the subject of extensive publication in materials science for the last six decades. These phenomena include nucleation, grain growth, coalescence and coarsening, and second phase formation. There has been work done to connect and scale these phenomena to generate a bigger picture, and it is the aim of this thesis to add to this work.

Specifically, structural analysis of dendritic microstructure and late-stage liquid pools following coalescence are discussed in the context of identifying the spatial and size distribution

of second phases formed during coalescence. This will be addressed by using phase field simulations and size analysis algorithms that will aim to reduce and present the problem in its bare bones form.

The remaining parts of this thesis are organized as follows:

- Chapter 1: Review of Solidification Theory – Basic concepts are outlined. Thus, a basic framework will be set up, allowing for the author to elucidate phenomena that are the subject of this thesis.

- Chapter 2: Problem Statement & Goals– Based on the review in the previous chapter, gaps in solidification where this thesis will focus on are identified. A problem statement is formalized with industrial manufacturing in mind to give purpose to research in these areas. Lastly, some goals are stated that capture the bigger picture that the author visualizes the sequel to this work to expand into.

- Chapter 3: Background – Some key studies are outlined. The aim here is to comment on some original work that the author finds relevant, and to point out shortcomings that this thesis will address.

- Chapter 4: Methods Background – Quantitative details that will equip the reader to grasp the tools used in this thesis are outlined in this chapter. These quantitative details pertain to the phase field model used to simulate microstructure, the phenomena of nucleation and techniques used to analyze microstructure.

- Chapter 5: Results and Discussion – The techniques described in the previous chapter are applied to characterize simulated solidification microstructure. The results' implications are discussed in the context of liquid pooling and second phase formation, and suggestions for future work made.

- Chapter 6: Conclusions – A brief summary of the entire thesis is presented.

CHAPTER 1 – REVIEW OF SOLIDIFICATION THEORY

Solidification, in its most basic form, is best visualized as the transformation of liquid to solid. This is a *phase* transformation, where the atomic-scale structure of the same substance changes. It is driven by an external temperature change, and the temperature at which this transformation begins is known as the freezing/melting temperature. This temperature change is accompanied by the extraction of latent heat from a liquid into the surrounding environment. In this process, heat is continuously redistributed during the process.

Solidification in any system undergoing a first-order phase transformation begins as tiny seeds/clusters of solid, separated from each other, which then grow -often in the pattern of beautiful snowflakes called dendrites- until they meet and merge with each other. This merger can be dynamic in its nature, resulting to the creation of grain boundaries at low enough concentrations or secondary phases when inter-dendritic liquid is at a sufficient concentration so as to trigger their nucleation. When this happens, the process of solidification is considered complete, and solid-state processes begin.

Formally, this process is summarized as follows:

- Solid seed formation – *Nucleation*
- Growth of solid seeds – *Free (Dendritic) Growth*
- Merger – It is this merger phenomenon that this thesis expands upon. This merger phenomenon can itself be broken down into constitutive processes:
  - There is an *initial coarsening* process, when the growing solid snowflakes interact with each other via impingement of their temperature and concentration fields. Snowflake arms thicken and some may coalesce.
  - *Coalescence* follows, which is the merging of dendrites to form a coherent solid network.

o   If the temperature remains close to the freezing temperature during coalescence, i.e. cooling rate is low, then there may be further *solid-state coarsening* and merging of dendrite arms, and the liquid pools that surround them.

1.1 – SOLIDIFICATION IN PURE SYSTEMS VS. ALLOYS

The phenomena associated with the solidification process described above pertain to both pure and alloyed materials. In alloys, the removal/redistribution of impurities is analogous to the redistribution of heat in pure materials. Therefore, well-accepted equations that describe redistribution of heat in a pure material solidification can also be used analogously to describe the redistribution of impurities in binary alloys. There is thus an analogy between solidification of pure materials and isothermal solidification in binary alloys. If the equilibrium value of one or more thermodynamic variables is plotted as a function of intensive variables, a *phase diagram* is obtained. In pure systems, a phase transition is an atomic re-arrangement process. On the phase diagram, different phases are represented by lines that separate different arrangements/phases. In alloy systems, a phase transition *may* involve an atom re-arrangement process. However, it also involves transfer of impurities from one phase to another. Examples of pure material and alloy phase diagrams are given below in Figure 1:
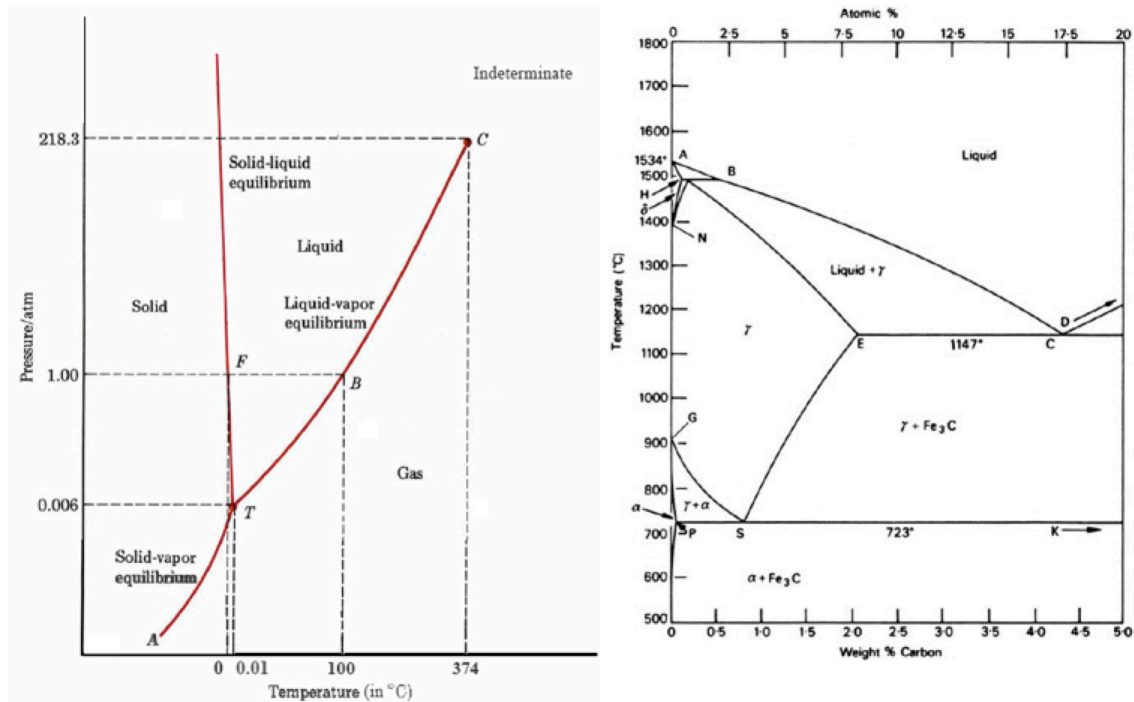
Figure 1–PHASE DIAGRAMS FOR WATER (LEFT) AND IRON-CARBON ALLOY (RIGHT)

The phenomena that characterize solidification are described in the following sub-sections in a comparative manner to outline the indiscriminant fundamental processes that create and drive them.

1.1.1 – NUCLEATION

For solidification to begin, formation of tiny solid seeds/clusters has to occur. These precursors to nuclei form due to movement of atoms driven by tiny thermal fluctuations of the stochastic kind, inherent in any system at non-zero temperature. They are responsible for randomly bringing about tiny groups of atoms in arrangements that are representative of a solid phase. At any given temperature, there is a probability distribution of possible sizes of these clusters, given by:

$$\frac{N_{nuc}}{N_l} = \exp\left(-\frac{\Delta G_{nuc}}{k_B T}\right)$$

<div align="right">**Eq. 1**</div>

where N_{nuc} is the number of clusters of some arbitrary size, N_l is the total number of atoms in the solidifying system, ΔG_{nuc} is the free energy of a cluster containing n atoms, k_B is the Boltzmann constant and T is the temperature of the system. Because this distribution pertains to a temperature driven phenomena, it derives from Boltzmann statistics.

An external temperature change, $\Delta T = T_2 - T_1$, where $T_2 < T_1$, causes a shift in this cluster size probability distribution. A driving force for nucleation is generated whenever T_2 is lower than the melting temperature. Below the melting temperature the liquid becomes metastable and $\Delta G_{l\to s}$ becomes negative, which implies an energetically favorable reaction. However, a nucleation event creates an interface between the liquid and solid bulk phases. This interface creation costs energy. Therefore, the total free energy change associated with a nucleation event in the bulk can be written as:

$$\Delta G_{nuc} = \frac{4}{3}\pi r^3 \Delta G_{l\to s} + 4\pi r^2 \gamma_{sl}$$

<div align="right">**Eq. 2**</div>

where γ_{sl} is the solid – liquid interfacial energy. These competing contributions amass to a critical threshold for the energetics and size/radius of a cluster, given by:

$$r_{nuc}^* = \frac{-2\gamma_{sl}}{\Delta G_{l\to s}}$$

<div align="right">**Eq. 3**</div>

and

$$\Delta G_{nuc}^* = \frac{16\pi\gamma_{sl}}{\left(\Delta G_{l\to s}\right)^2}.$$

<div align="right">**Eq. 4**</div>

ΔG^{*}_{nuc} is frequently called the 'activation energy' of nucleation. These can be found by setting

$\frac{dG_{nuc}}{dr} = 0$ and solving for r.
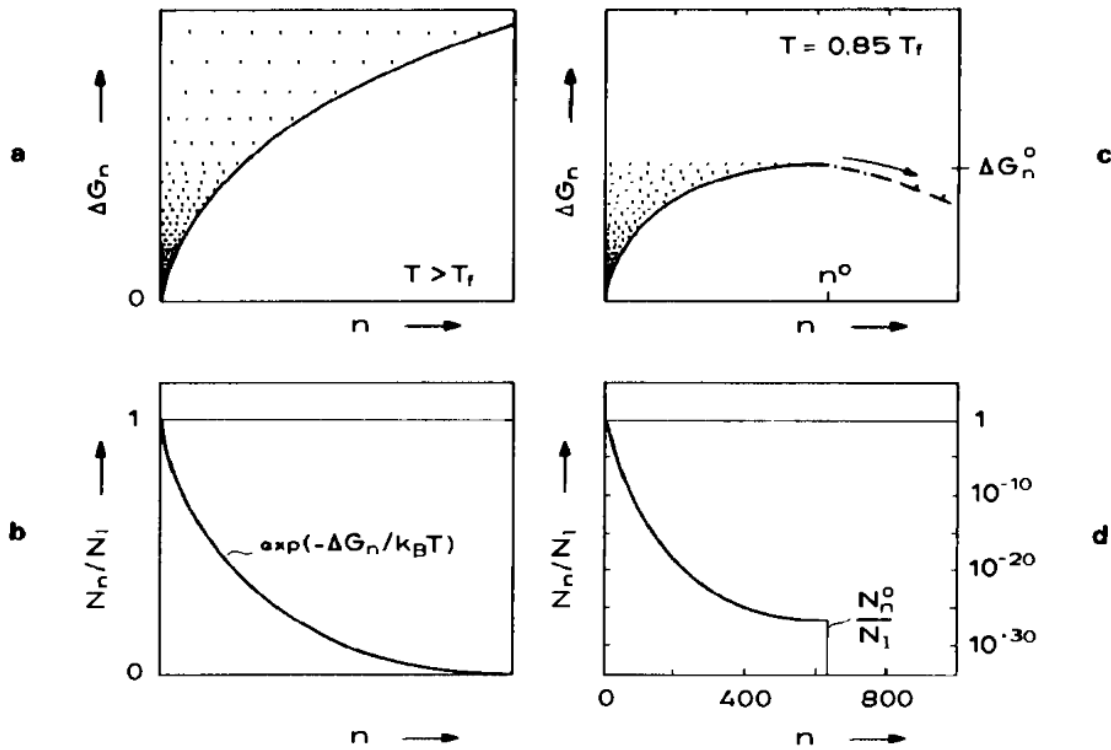
Figure 2 - DEPENDENCE OF CLUSTER SIZE DISTRIBUTION ON TEMPERATURE(Fisher & Kurz, 1998)

Nucleation events are classified into two types:

- *Homogenous* – Nucleation in bulk liquid
- *Heterogeneous* – Nucleation on a substrate

Equations 6 through 8 describe homogenous nucleation. Therefore ΔG_{nuc}, ΔG^{*}_{nuc} and r^{*}_{nuc} can be effectively labeled ΔG_{hom}, $\Delta G^{*}_{\mathrm{hom}}$ and r^{*}_{hom}. Heterogeneous nucleation is much more common, and occurs on a substrate, usually present in melts in the form of impurities or added

inoculants. These impurities/inoculants effectively lower the $\Delta G^{*}_{\mathrm{hom}}$, which implies a lowering of the cost of creation of an interface, i.e. the effective surface energy is lowered. This effect can be expressed through a heterogeneous factor given by:

$$f(\theta) = \frac{(2+\cos\theta)(1-\cos\theta)^2}{4}$$

Eq. 5

where θ is the wetting angle between the substrate and the cluster/nucleus.

Thus,

$$\Delta G_{het} = \left(\frac{4}{3}\pi r^3 \Delta G_{l\to s} + 4\pi r^2 \gamma_{sl} \right) f(\theta)$$

Eq. 6

which implies that:

$$r^{*}_{het} = \frac{-2\gamma_{sl}}{\Delta G_{l\to s}}$$

Eq. 7

and

$$\Delta G^{*}_{het} = \frac{16\pi\gamma_{sl}^3}{3\left(\Delta G_{l\to s}\right)^2} f(\theta)$$

Eq. 8

This implies that the critical size/radius of the cluster/nucleus is independent of the type of nucleation. It suggests that for a given γ_{sl}, $\Delta G_{l\to s}$ and thus the undercooling ΔT determines the nuclei density for any solidification process, and by extension, grain density. Athermal nucleation in 4.1.2 will expand on this discussion.

Although the derivation above pertains to pure systems, it can be extended to systems with more than one component, i.e. alloys. This can be done by allowing the energetics to vary not only with cluster/nucleus size, but also with composition. In this case, the critical thresholds can be found by setting:

$$\frac{dG_{nuc}}{dr} = 0 \qquad\qquad \text{Eq. 9}$$

and

$$\frac{dG_{nuc}}{dc} = 0 \qquad\qquad \text{Eq. 10}$$

where c is the nucleus composition. The energy can then be visualized as a landscape, with the critical threshold defining a saddle point.

By extension of the arguments presented above for the cluster probability distribution, the rate of formation of nuclei, i.e. the nucleation rate, can also be expected to follow Boltzmann statistics. A cluster of critical size only becomes a nucleus upon further attachment of atoms, which is also a thermally activated process. Therefore, the nucleation rate can be imagined to be the sum of two successful events: formation of a cluster of critical size and growth of the cluster by further attachment of atoms. This argument was first made by Volmer and Weber(Volmer & Weber, 1926) and is mathematically represented as follows:

$$\dot{N} = N_l \exp\left(-\frac{\Delta G_{nuc} + \Delta G_{att}}{k_B T}\right) \qquad\qquad \text{Eq. 11}$$

where $\dot{N}$ is the nucleation rate, ΔG_{att} is the activation energy associated with competing energetics of surface creation and bond formation for atom attachment.

Equation 11 pertains to the homogenous nucleation rate. It can be transformed to the heterogeneous nucleation rate by the addition of the heterogeneous factor:

$$\dot{N} = N_l \exp\left(\frac{-\Delta G_{nuc} f(\theta) + \Delta G_{att}}{k_B T}\right) \qquad\qquad \text{Eq. 12}$$

Near the melting temperature, $\Delta G_{l \to s} = G_l - G_s$ can be approximated by $\dfrac{L\Delta T}{T_m}$. This means that the

ΔG_{nuc} term displays a $-\dfrac{1}{T\Delta T^2}$ behavior while the ΔG_{att} term displays a $-\dfrac{1}{T}$ behavior. This

leads to a maximum in the nucleation rate being observed, where the rate of clusters becoming

nuclei and atoms attaching to these nuclei is at its highest.

Zeldovich (Zeldovich, 1943) proposed an updated version of nucleation rate equation:

$$\dot{N} = Z\beta N_l \exp\left(-\frac{\Delta G_{nuc}}{k_B T}\right)$$

Eq. 13

where β is the attachment frequency which encompasses the ΔG_{att} term and Z is the Zeldovich

Factor that incorporates the probability of decay of critical sized clusters into smaller sizes

(growth of a cluster is a reversible reaction). Equation11 does not account for this decay.

As with equation 11, Zeldovich's updated nucleation rate can also be extended to

heterogeneous nucleation:

$$\dot{N} = Z\beta N_l \exp\left(-\frac{\Delta G_{nuc}}{k_B T} f(\theta)\right)$$

Eq. 14

1.1.2 – FREE GROWTH

Upon nucleation, growth of nuclei having snowflake patterns are usually observed.

Formally, this snowflake form of growing solid nuclei is referred to as a dendritic structure, and

this structure determines properties of a solidified system. For instance smaller dendrites

generally lead to an increased ductility in an alloy.

The exquisite nature of this dendritic structure has been the subject of much fascination

and study, and it is best described in terms of a Stefan problem. The problem is named after Jožef

Stefan, a Slovene physicist, and it describes a phase boundary that can move with time. It is

particularly applicable in the case of a homogeneous medium going through a phase change, i.e.

solidification. This formulation consists of a partial differential equation (PDE), which describes this moving phase boundary in time.

The driving force, a temperature change, that causes expulsion/redistribution of (latent) heat, is given by:

$$\rho c_p \frac{\partial T}{\partial t} = k\nabla^2 T \qquad\qquad \text{Eq. 15}$$

where ρ is the density, t is time, c_p is the volumetric heat capacity, and k is the thermal conductivity. Equation 15 is applied twice, once in each phase and assumes equal values of ρ, c_p, and k in each.

The physics of the problem dictate that at the solid – liquid interface, the temperature field remain continuous *and* energy be conserved.

Respectively,

$$k\frac{\partial T}{\partial t}\bigg|_s - k\frac{\partial T}{\partial t}\bigg|_l = L_f v_n \qquad\qquad \text{Eq. 16}$$

and

$$T_i \equiv T_s \equiv T_l = T_m - \Gamma\kappa - \beta v_n \qquad\qquad \text{Eq. 17}$$

where $L_f^{l \to s}$ is the latent heat of fusion expelled at the interface, v_n is the velocity of the interface to the normal direction, T_s and T_l are the temperatures on the solid and liquid side of the interface, T_m is the melting temperature of the pure material, and β is a kinetic coefficient that captures the properties of the interface at v_n. Γ is the Gibbs Thomson constant, which captures the effect of curvature on the temperature across an interface. The Gibbs-Thomson effect is expanded upon in the next section, 1.1.3. The Gibbs-Thomson coefficient is defined as:

$$\Gamma = \frac{T_m \gamma_{sl}}{L_f^{l \rightarrow s}} \qquad \text{Eq. 18}$$

The description above pertains to pure systems. An analogous description can be derived for binary alloys as per the arguments at the beginning of section 1.1. For a binary alloy, the PDE description is altered to account for impurity concentration, i.e.:

$$\frac{\partial c}{\partial t} = D_l \nabla^2 c \qquad \text{Eq. 19}$$

where D_l is diffusion coefficient of the impurity in the liquid, and c is the concentration of the impurity in the liquid. The temperature field is assumed constant, since heat is assumed to diffuse much faster, rendering the need for a PDE of the kind relevant to pure systems irrelevant. The PDE for impurity concentration also assumes zero diffusivity in the solid, since liquid diffusion may be orders of magnitude larger relative to solid diffusion.

Boundary conditions to be satisfied in this case require zero impurity flux. At the solid – liquid interface continuity *and* conservation of the concentration field are required:

$$D_l \nabla_n c = c(1 - k)v_n \qquad \text{Eq. 20}$$

and

$$c_l = \frac{c_0}{k} - \frac{\gamma_{sl} T_m}{|m_l| L_f} - \beta v_n \qquad \text{Eq. 21}$$

where c_l and c_s are the concentrations on the solid and liquid sides of the interface respectively, c_0 is the average composition of the alloy, m_l is the liquidus slope, κ is the local radius of curvature, and k is the partition coefficient as given by the equilibrium phase diagram for the binary alloy, defined as follows:

$$k = \frac{c_s}{c_l} \qquad \text{Eq. 22}$$

The equations listed above describe a dilute binary alloy, and track the solidification process by keeping track of the phase boundary. The phase boundary (from now on referred to as the *interface*) is assumed to be of zero thickness. Therefore, it can be imagined to be atomically smooth. The Stefan problem has therefore come to embody what is now known as the sharp interface model. Numerically, these models are hard to implement. The interface needs to be explicitly tracked, and complex topological features of the dendritic structure of several growing nuclei are hard to capture accurately. This is especially true during merger. Also, an atomically smooth interface is an unrealistic feature in solidifying binary alloys, i.e. it has a finite width usually on the order of nanometers.

A more recent class of models known as *Phase Field* models address these concerns, and one such model has been used to simulate microstructure for this thesis. The phase field model is described in section 4.1.1.

1.1.3 – MERGER: COARSENING& THE SUBTLE DIFFERENCES BETWEEN FUNDAMETALLY SIMILAR PHENOMENA

As the growing nuclei, called grains herein, close in on each other, they undergo a process known as coarsening. This process is analogous to that where tiny oil droplets suspended atop a liquid coming together to form big ones, whereby bigger droplets grow at the expense of smaller ones. Formally speaking, coarsening is the growth of bigger droplets or *particles* at the expense of smaller ones.

Coarsening is driven by the Gibbs-Thomson effect, which is the establishment of a pressure differential across a *curved* boundary/interface. This leads to an energy differential known as a *chemical potential* differential, and it makes systems exhibiting it unstable. Therefore, a driving force to move away from this unstable state is established. In other words, a system exhibiting the Gibbs- Thomson effect changes so as to lessen/eliminate the effect. In pure materials, this chemical potential differential manifests itself as a pressure differential, whereas in impure materials such as binary alloys it appears as an impurity concentration differential. The

Gibbs – Thomson effect, formalized by equation 18 in section 1.1.2, is stronger for higher curvature, so in the scenario depicted above, the smallest of oil droplets would be most unstable and disappear first. So on and so forth until the chemical potential differential is eliminated.

It is beneficial at this point to summarize the three related phenomenon that the author considers to fall under the umbrella of coarsening and merger process. The author also feels that most literature and materials science texts do not deal with subtle differences adequately.

Coarsening can manifest as three processes in a solidifying system:

- *Ripening* — this is seen as smaller dendrite arms melting to deposit themselves onto larger arms, resulting in a smaller number of dendrite arms. It also leads to an increase in average dendrite arm spacing. This was described above.
- *Coalescence* –this is seen as agglomeration of dendrite arms when matter diffuses preferentially onto solid regions of stronger negative curvature. It is driven by curvature, thermodynamic driving force and the solid-liquid versus solid-solid grain boundary energy differences. Like in ripening, this process also leads to an increase in average dendrite arm size(Mortensen, 1989).
- *Grain coarsening* –this is seen as redistribution of solid network of grains from smaller grains onto bigger ones, leading to an increase in the average grain size. This process can be driven by the ripening kinetics described above as well as (in pure materials) solely the elimination of interface curvature.

In all three flavors of coarsening, the characteristic features are an increase in feature size, and result in a proportional decrease in the amount of interface present in a system. This change in size of characteristic features shows interesting scaling dynamics, in which the features at late times at large scales are statistically similar to earlier times at smaller scales. Great consideration therefore has been given to characteristic lengthscales that describe evolution of features in a solidifying system. A very brief description of this lengthscale evolution is presented below.

An example of lengthscale evolution is the increase in grain size when a solidified system is subjected to a high temperature, where the average grain size increases to minimize surface energy by decreasing interface area. This is because interface creation costs energy, which was pointed out in the previous section. Therefore the rate of change of grain size is large for large amount of interface present in the system. Conversely, a large amount of interface is accompanied by small grains. Therefore rate of change of grain size is inversely proportional to average grain size:

$$\frac{d}{dt}\left(\overline{d}\right) = K\frac{1}{\overline{d}} \qquad \text{Eq. 23}$$

where K is a proportionality constant dependent on time. Therefore the time taken to reach a particular grain size is given by the solution of equation 23 above:

$$\overline{d} - \overline{d}_0 = Kt^{\frac{1}{2}} \qquad \text{Eq. 24}$$

where the time exponent is indicative of kinetics. A time exponent of size half represents *volume* diffusion limited kinetics, and gives a *parabolic growth law*.

Dendritic coarsening occurs through matter transport in a finite liquid medium, therefore *surface* diffusion limited kinetics are expected to be at play. This has been confirmed through experimental measurements of exponents of around ⅓.In reality, the diffuse nature of the collective measurements underpins a departure from ideal conditions. In other words, it indicates a mixture of transport mechanisms at work at any given point in time(J. Cahn, 1962; Glicksman, Smith, Marsh, & Kuklinski, 1992; Grey & Higgins, 1973; Kailasam, Glicksman, Mani, & Fradkov, 1999).

Henceforth, the comparison between pure and alloys stops, and this thesis will deal only with the more complex case of binary alloy solidification.

CHAPTER 2 – PROBLEM STATEMENT

The phenomena described in Chapter 1 underpin all solidification microstructure, which in turn determines properties of alloys. Therefore, ever better control of microstructure gives purpose to all materials science research. Notably, the aerospace industry has demanded increasingly stronger alloys while simultaneously attempting to reduce weight for energy efficient vehicles. This has been accomplished in two principal ways: newer heat treatments and increasing the concentration of/adding alloying elements. Both of these result in a change in grain boundary segregation. This leads to additional constituents, dispersoids and precipitates, i.e. second phases, in the microstructure. Such phases are desirable as they are either the cause of strengthening, or act as precursors for strengthening phases that appear downstream during post-processing. Some second phases however are unwanted as they cause hot tearing, reduction in durability and fracture toughness, etc.(Starke & Staley, 1996).For e.g., Figure 3 shows how the number density of precipitates affects strength in 2090 alloys.
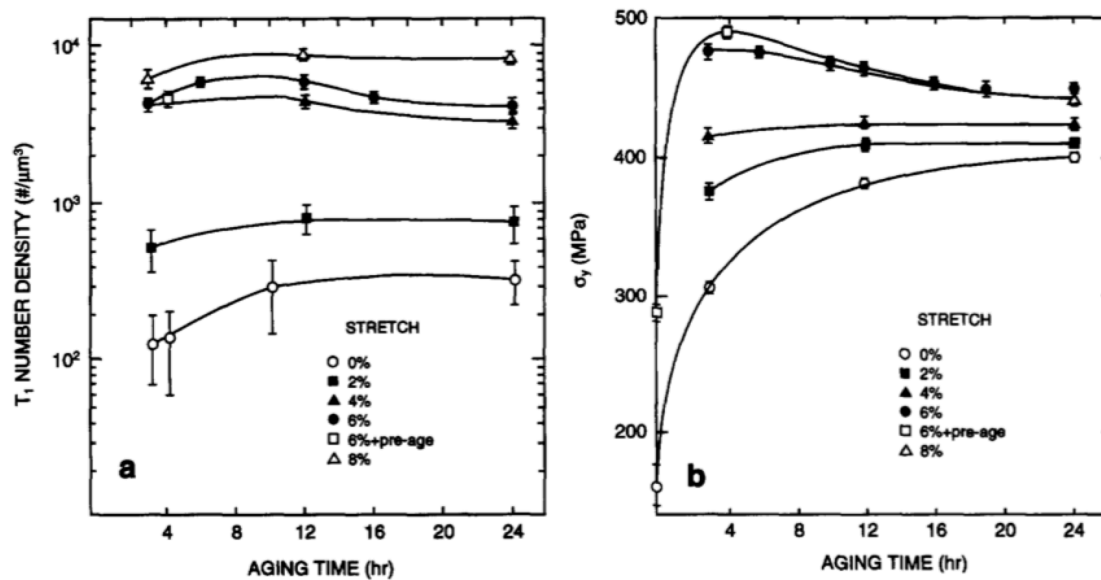
Figure 3 - RELATION OF PRECIPITATE DENSITY AND YIELD STRESS(Starke & Staley, 1996)

Specifically, it has been found that the size and distribution of second phases drastically affects the desired properties. Not surprisingly, this connection is quite intimate and complex. In order for has been postulated that by understanding this connection, better control over industrial manufacturing can be achieved(Heinz et al., 2000; Mikhaylovskaya, Ryazantseva, & Portnoy, 2011; Quested & Greer, 2004).

There has been work done to quantify the size distribution of second phases in alloys, but the employed approach has always been *investigative* rather than *predictive*. A common technique is to dissolve the primary phase away, leaving behind the second phases that are then analyzed(Lu, Wiskel, Omotoso, Henein, & Ivey, 2010). Some of this work is reviewed in the next chapter.

This thesis aims to adopt a predictive approach to understanding length scale selection in the topology of second phase sites during late stage solidification. It highlights analysis of liquid pooling evolution and structure during the late stages of solidification. These liquid pools are the precursors for the first second phases to form. Consequently, a working assumption made here is that the structure of these late stage liquid pools is very similar to that of the first second phases to form. Due to this similarity, it is hypothesized that the sizes and distribution of second phases can illuminated by studying the structure of their precursors, i.e. late stage liquid pools. In particular, the effect of cooling rate on liquid pool evolution will be examined. The argument for this thesis' hypothesis is visually depicted in Figure 4.
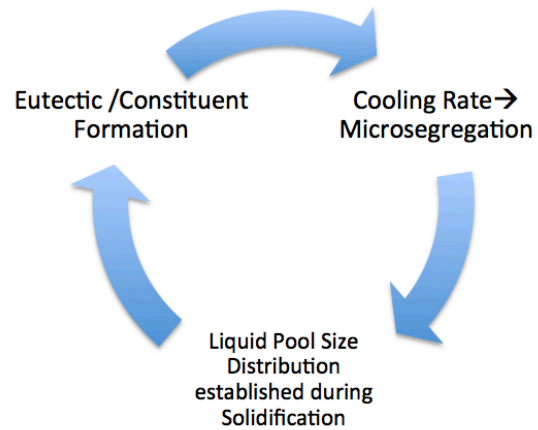
Figure 4 - HYPOTHESIS FOR THIS THESIS

This thesis also aims to be a first step towards a longer-term goal, which is to obtain a theory that correlates liquid pool evolution to second phase formation. Such a theory will then truly act as a predictive tool.

CHAPTER 3 – BACKGROUND

To create a backdrop for the analysis presented in this thesis, this chapter highlights and critiques some studies. The aim throughout is to keep in touch with the problem statement and goals discussed in the previous chapter.

The effects of second phase sizes and distributions are briefly discussed along with associated experimental techniques. This chapter then adopts a computational tone, and examines some work done to simulate early second phase growth on a sizable scale. A novel analysis technique that is exploited for results in this thesis is also reviewed.

Finally, in the context of the long-term goals proposed in the previous chapter, some thermodynamic and scaling observation about liquid pool topology are made that lay ground for future work.

3.1 – EXPERIMENTAL DETERMINATION OF SECOND PHASE SIZES AND DISTRIBUTIONS

Optical techniques have been the norm for analysis of microstructure, and are well suited within a laboratory context. They have been used to determine a wide variety of features such as grain size, second phase sizes and distributions, thickness of coatings, etc. Results of such analysis are usually averaged over multiple locations in many samples of the same microstructure. Such techniques are also time consuming, and may not be useful in a manufacturing environment.

Matrix dissolution via chemical or electro-chemical dissolution is a popular technique for obtaining quick and reliable results to characterize second phase particles. It is quite challenging due to the fact that some second phases dissolve more readily than others. Therefore a host of chemical procedures exist to extract such particles. The extracted particles are identified using Energy Dispersive Spectra. Size distributions of the extracted particles are obtained using Transmission Electron Microscopy. The sequence of methods described above remains more or less uniform across various studies. Such analysis remains investigative rather than predictive.

The reader is directed to references(Ekström, Hagström, & Östensson, 2000; Gupta, Marois, & Lloyd, 1996; Lu et al., 2010)for relevant examples.

3.2 – COMPUTATIONAL SIMULATION OF MICROSTRUCTURE ON A SIZEABLE SCALE

In addition to identifying the second phases, there has been considerable interest in modeling second phase growth itself. In doing so, it is hoped that details of growth kinetics will elucidate growth modes of, for e.g. second phases of the eutectic kind. Different growth modes lead to different eutectic structures that vary in size and distribution, which in turn dictates properties and downstream processing (Dahle, Lee, & Nave, 2001).

The Cellular Automaton (CA) technique has been an attractive avenue for simulating systems on a large scale to study realistic problems. The idea behind a CA model is to define a volume or a grid of cells, where each cell is in a particular state. The cells can change states reversibly or irreversibly using a pre-defined set of transition rules. Khajeh and Maijer(Khajeh & Maijer, 2010) employed the CA technique to study the case of solidification. Here, the possible cell states are solid, liquid and eutectic. Primary dendritic solidification microstructure can then be determined dynamically by assigning the appropriate number of cells to solid. In(Khajeh & Maijer, 2010)the initial primary structure was obtained from solidification experiments using x-ray microtomography performed on Al-Cu alloys with 20-wt% Cu. The alloys were quenched after the start of eutectic transformation, seen via the measured temperature, to lock in the primary structure for the x-ray microtomography.

A nucleation and growth algorithm was then employed to simulate the eutectic growth in the liquid pools regions. The number of active nuclei per unit volume, i.e. clusters that have grown to become nuclei, is given by:

$$N_v = \beta_1 \Delta T^{\beta_2} \qquad \text{Eq. 25}$$

where β_1 and β_2 are fitting parameters that depend on the alloy type, and ΔT is the local undercooling.

The growth of eutectic nuclei is driven by:

$$\frac{dR}{dt} = \beta_3 \Delta T^2$$

<div align="right">**Eq. 26**</div>

where R is the radius of the eutectic grain and β_3 is a growth coefficient unique to the alloy. These coefficients were determined using a least squares fit from experimental data. The results of their simulations are shown in Figure 5. Here, grey represents primary phase, and every other color is a unique eutectic grain.
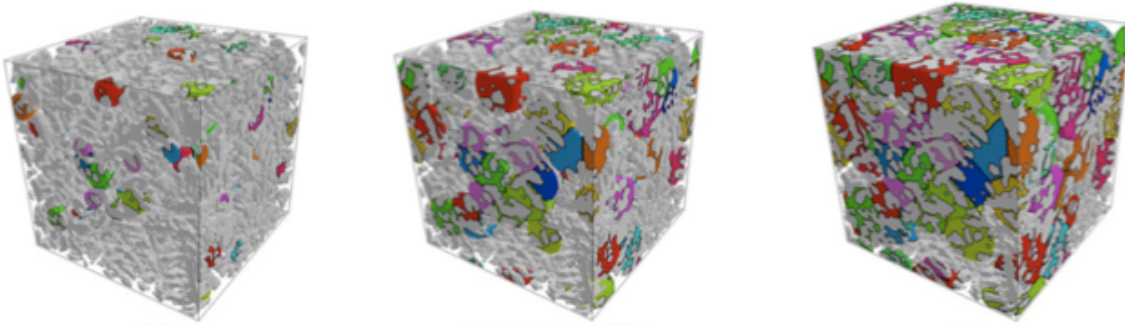
Figure 5 - 3D REPRESENTATION OF MICROSTRUCTURE OBTAINED FROM CA STUDY(Khajeh & Maijer, 2010)

This study takes first steps in envisioning a process that would try and look at structure on a larger scale in order to analyze microstructure spatially. However, it doesn't present such analysis, and limits itself to prediction of diameter of eutectic grains and the eutectic grain density. Additionally, their initial condition/microstructure determined from x-ray microtomography essentially put in the answer regarding the second phase topology '*by hand*'. The assumption is that the eutectic transformation starts at a temperature determined through an Scheil-Gulliver approach, which assumes no diffusion in the solid. This is inaccurate, and a finite solid diffusion coefficient has been shown by Ofori-Opoku et al.(Ofori-Opoku & Provatas, 2010; Rappaz, Jacot, & Boettinger, 2003) to be necessary for coalescence and closure of grains. Lastly,

the experiments were carried out at low cooling rates, it remains questionable whether their approach/results can be used for any cooling rates to determine large-scale structure of second phases.

3.3 – A THERMODYNAMIC ARGUMENT FOR EVOLUTION OF LIQUID POOLS AND SUBSEQUENT FORMATION OF SECOND PHASES

It was pointed out in the CA study outlined in the preceding section that the determination of the start of the eutectic transformation was sufficiently arbitrary due to lack of consideration of the effect of back diffusion. Notably, back-diffusion serves to alter the concentration of solute in the late-stage liquid (also known as microsegregation), and also allows for additional coarsening during closure. Coarsening has been shown to play an important role in determining the final scale of microstructure (Prasad, Henein, Maire, & Gandin, 2006), and by extension, can be expected to play a major role in spatial distribution of liquid pools and second phases. To address this shortcoming, it is important to consider the microsegregation that precedes formation of any second phase.

D. V. Malakhov et al.(Malakhov, Panahi, & Gallerneault, 2010) showed that the conditions for nucleation for any arbitrary second phase are two fold:

1. A positive driving force for nucleation
2. *Compositional similarity* of the nucleating phase to the liquid.

If there are multiple second phases that can form in a late-stage liquid pool, for e.g. in a multicomponent alloy at *high cooling rates*, then the second condition strongly influences *which* second phase nucleates. This argument is visually depicted in Figure 6.
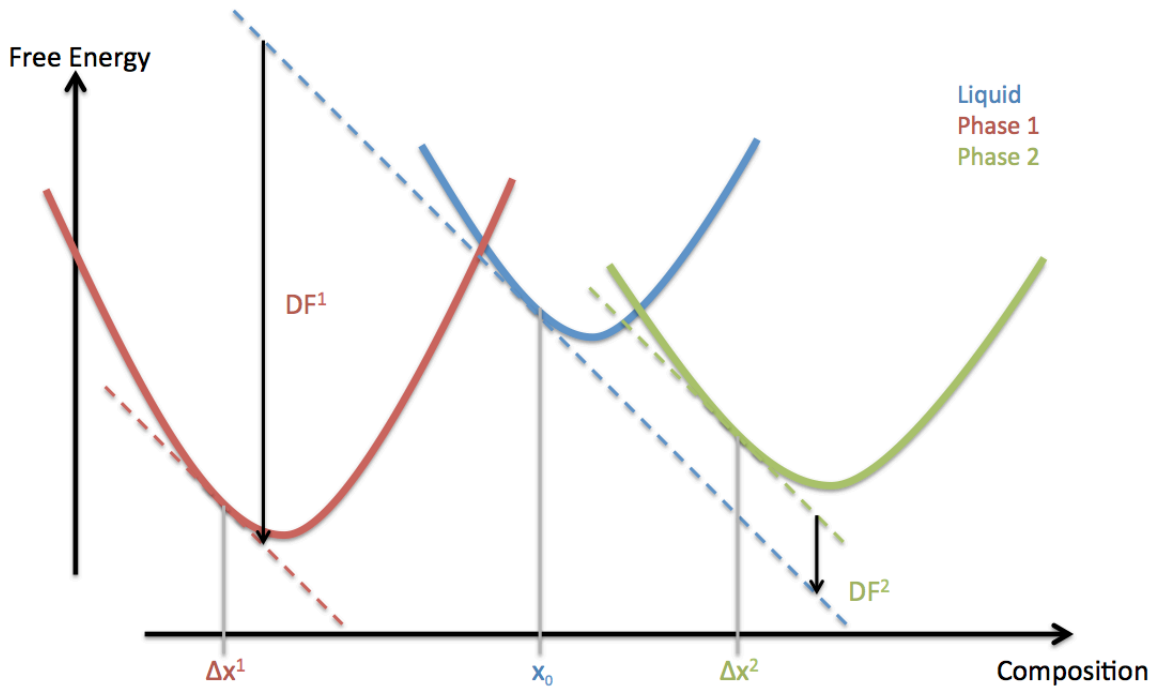
Figure 6 - INTERPLAY BETWEEN DRIVING FORCES AND COMPOSITIONAL SIMILARITY

The driving force for formation of any second phase i can be calculated as follows:

$$DF_i = G_L - G_i + (x_i - x_0)\left(\frac{\partial G_L}{\partial x_L}\right)_{x=x_0}$$

Eq. 27

where G_L and G_i are the molar Gibbs energies of the liquid and the second phase respectively, x_0 is the average composition of the liquid, and x_i is the equilibrium composition of the second phase.

Compositional similarity can be measured in terms of Euclidean distance:

$$\Omega = 1 - (x_i - x_0)^{\frac{1}{2}}$$

Eq. 28

In Figure 6, phase 2 would be expected to form in preference to 1 if cooling rates were high enough. This is because phase 1 is compositionally similar to the liquid pool, despite having a

lower driving force of formation. The preferential formation of phase 2 as opposed to phase 1 reflects rapidly decreasing mobilities, and it becomes energetically more favorable for liquid to partition into a compositionally similar phase.

In multicomponent alloys, driving forces for multiple second phases become positive at high cooling rates. Most of these second phases are of the metastable kind, which are not predicted by the equilibrium phase diagram. Therefore expected amounts of second phases using equilibrium conditions do not match the amounts found in industrial casts. Malakhov et al. showed that the change in segregation behavior at high cooling rates is significant enough to allow driving forces for metastable phases to become positive. Using the compositional similarity argument Malakhov et al. were able to accurately predict and experimentally validate the formation of metastable phases.

Bringing the CA study back into focus, at the start of the eutectic transformation its subsequent growth mode (fibrous or lamellar) is affected by cooling rates and the resulting change in microsegregation. To accurately predict second phase growth selection, alongside sizes and distributions, this change in microsegregation must thus be considered.

With regards to the long-term goal of a theory that correlates liquid pool evolution and second phase formation, compositional similarity can be expected to play a major role. Consequently, models that capture microsegregation dynamics with changing cooling rates accurately are crucial in any study that hopes to connect liquid pool evolution to second phase formation.

3.4 – AN ARGUMENT FOR EXISTENCE OF SCALABLE BEHAVIOR OF LATE-STAGE LIQUID POOLS

Coarsening, which drives late-stage liquid pool evolution, has been shown to exhibit a scaling behavior. As outlined in section 1.1.3, it comes in many flavors.

The classic analysis of Lifshitz and Slyozov (Lifshitz & Slyozov, 1961) showed a universal behavior in coarsening systems. In coarsening systems, the cube of the average of the radius is linearly dependent on time, according to:

$$\overline{R} = kt = \frac{4}{9}dDc_e t^{\frac{1}{3}} = \frac{8\sigma vDc_e}{9RT}t^{\frac{1}{3}}$$

Eq. 29

where k is the rate constant, d is the capillary length, D is the diffusivity of solute in the matrix phase, c_e is the equilibrium concentration of solute species across a flat interface, σ is the interfacial energy, v is the molar volume of the solute species in the coarsening phase and R is the gas constant.

This implies cube root kinetics, and an example of scaled size distributions that result from what is now known as the LSW theory is given in Figure 7. These distributions plot normalized particle size distribution P^* vs. reduced size $z^{\frac{1}{3}}$.
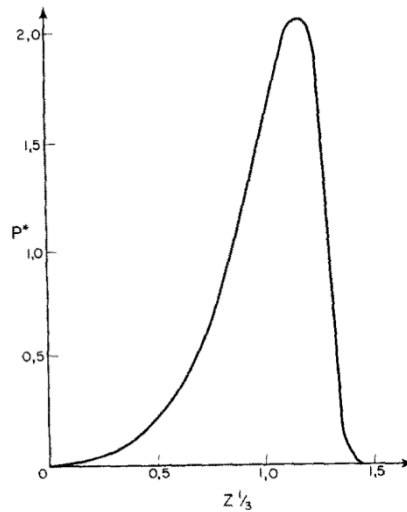
Figure 7 - SCALED SIZE DISTRIBUTION OBTAINED FROM LSW THEORY (Lifshitz & Slyozov, 1961)

Additionally, S. Gurevich et al. showed linear dependence on the cube root of time for the ripening and coalescence of liquid pools in directionally solidifying systems (Gurevich, Amoorezaei, Montiel, & Provatas, 2012).

Another notable contribution to the study of merger behavior comes from Aagesen et al. (Aagesen et al., 2010). Their analysis illustrates universal dynamics for merger in solidifying systems. Self-similar morphological features, i.e. the interface shape, are shown to follow cube root kinetics. Their results are shown in Figure 8. They show that a pinching event assumes a conical morphology (as shown in the thumbnails in figure 8). The conical morphology reduces in size in time, and the data can be scaled when time is plotted in a normalized fashion. A scaling exponent of ⅓ for time indicated coarsening processes predominantly active during a pinching event. Universality in this context implies that the interface shape is independent of initial conditions, and could potentially be used to determine the time needed for onset of liquid pool isolation.
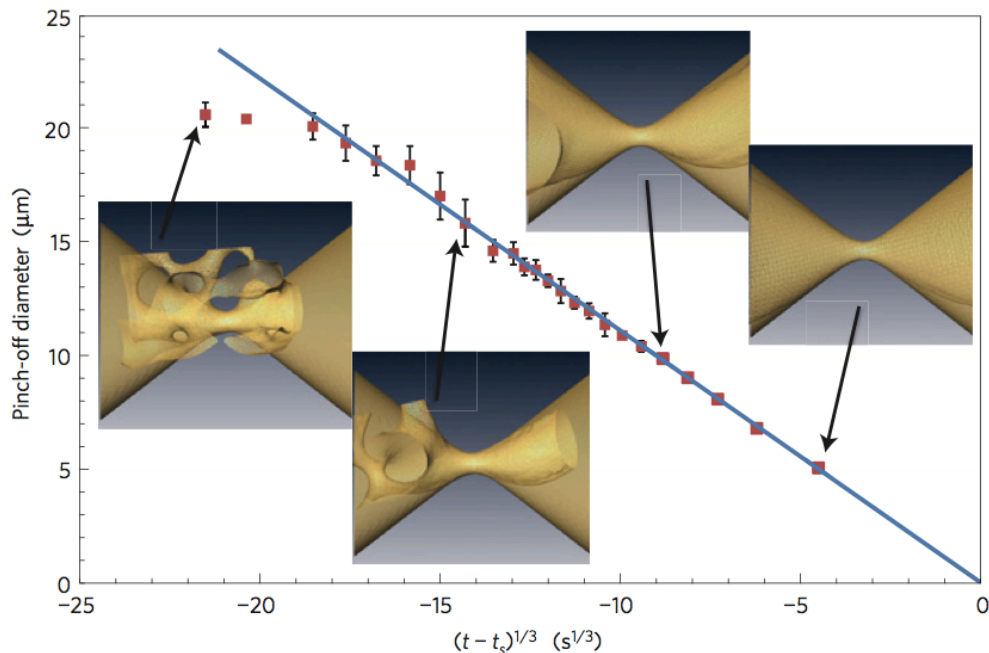
Figure 8 - UNIVERSAL DYNAMICS FOR MERGER BEHAVIOR(Aagesen et al., 2010)

The studies presented in this section hint to existence of an overall pattern/trend for liquid pool evolution. By extension, the structure of the initial second phases at least can also be expected to show some scalable behavior.

3.5 – A NOVEL TECHNIQUE FOR QUANTIFYING EVOLUTION OF MICROSTRUCTURE

One way of viewing late-stage liquid pooling is through the theory of percolation. Almost no attention has been given to the percolation transition in solidifying microstructures. The author, to the best of his ability, is aware of only one such study, highlighted subsequently.

The phase distributions is solidifying systems is correlated, where the correlations manifest in a highly networked structure. This arises from interaction of primary phase nuclei, either through soft impingement of diffusion fields or through '*hard*' impingement upon contact. Brunini et al.(Brunini, Schuh, & Carter, 2011) investigated the percolation transition with respect to system size for two kinds of phase transformations: spinodal decomposition and nucleation and growth (non-dendritic). Their results are shown for the nucleation and growth case in Figure 9. Different curves correspond to different system sizes, given by L, where a higher L indicates a bigger square system.
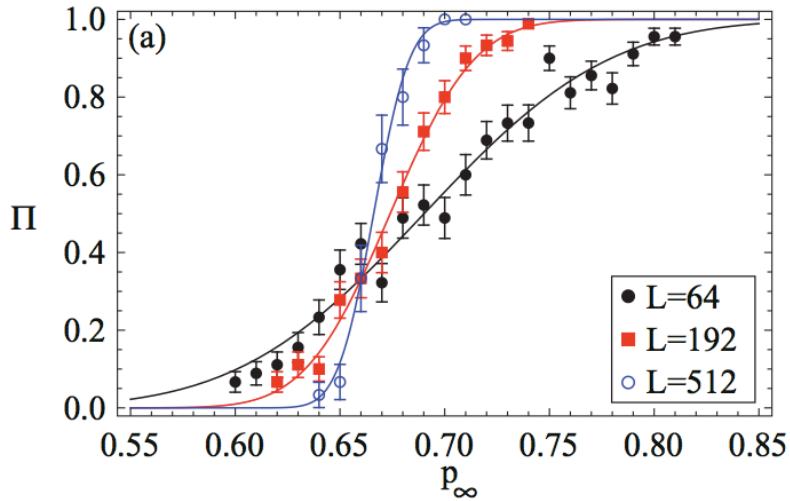
Figure 9 - PROBABILITY OF FINDING A SPANNING CLUSTER VS. PERCOLATION THRESHOLD(Brunini et al., 2011)

Their results were fitted to an error function of the form:

$$\Pi(p) = \frac{1}{2}\left[1 + \left(\frac{p - p_c^{eff}}{\Delta}\right)\right]$$

Eq. 30

where $\Pi(p)$ is the probability of finding a spanning cluster defined as the fraction of simulations containing a spanning cluster, p is the liquid fraction, p_c^{eff} is the effective percolation threshold in terms of liquid fraction for the phase in question defined as the intersection of the three curves shown above, and Δ is the width of the percolation transition which is defined as the liquid fraction for which the value of the error function lies between 0 and 1.

For the case of nucleation and growth, the percolation thresholds show an increase compared with the standard random lattice threshold. It is speculated to be due to the coarsening mechanisms at play throughout the growth process.

This speculation arises from a spatial correlation analysis, where the time evolution of a characteristic length obtained from pair correlation functions shows three regimes:

1. Independent growth at early times,
2. Coalescence of neighboring particles at intermediate times,
3. Self-similar coarsening process at late times.

The results from their spatial correlation analysis for the nucleation and growth case are shown in Figure 10. Chapter 5 uses these concepts to elucidate liquid pool evolution, which also displays a highly networked structure.

Figure 10 - PAIR CORRELATION FUNCTION VS.DISTANCE (TOP) AND GROWTH OF THE CHARACTERISTIC LENGTH SCALE VS. TIME (BOTTOM) (Brunini et al., 2011)

CHAPTER 4 – METHODS BACKGROUD

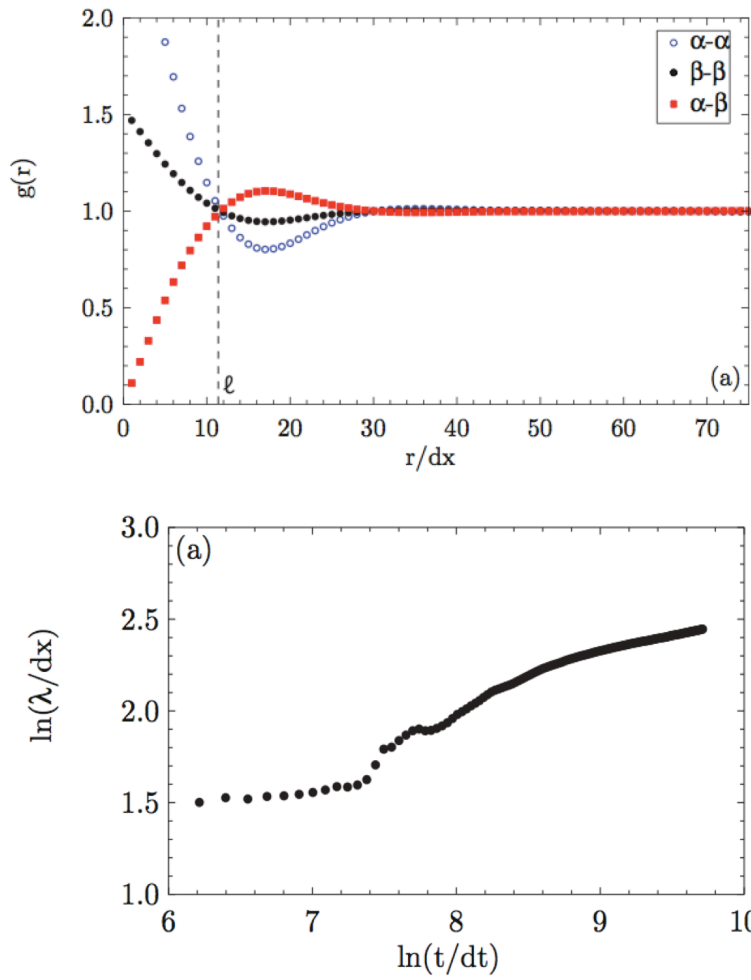In this chapter the phase field model used to simulate microstructure along with some of its features is discussed. In addition, techniques to analyze microstructure are highlighted and critiqued. Some thermodynamic and scaling arguments are also made that build upon the literature review in the previous chapter. These arguments will serve to elucidate some of the results present in Chapter 5.

4.1 – PHASE FIELD MODEL

The phase field method has been recognized as a powerful tool to model complex topological features, and phase field models that build on this method are ubiquitous in many scientific areas of study(J. W. Cahn & Hilliard, 1958; Hohenberg & Halperin, 1977; Rowlinson, 1979).

The phase field method allows for discrimination between different phases that may exist at identical temperatures, concentrations, etc., through an order parameter/field that has one value in one phase, and a second value in all others. Its principal characteristic is the presence of a diffuse interface, which is a realistic feature in solidifying systems. The method as it pertains to phase transitions was first formalized by Ginzburg and Landau, and was used by Cahn and Hilliard to model spinodal decomposition in their 1958 – 1959 series of papers(J. W. Cahn & Hilliard, 1958, 1959).

A phase field model can be constructed using physical arguments, where these physical arguments enter the model via a global free energy that describes the different phases' dependence on each other. For this thesis, a phase field model for a dilute binary alloy developed by Ofori-Opoku et al.(Ofori-Opoku & Provatas, 2010) is used that has been successfully applied to many alloy solidification studies(Amoorezaei, Gurevich, & Provatas, 2012; Gurevich, Amoorezaei, & Provatas, 2010; Ofori-Opoku & Provatas, 2010). The global free energy is given by:

$$F[\phi,c,T] = \int \left\{ \sum_{i=1}^{N} \frac{1}{2} \left| \varepsilon(\vec{\phi}) \nabla \phi_i \right|^2 (+ f(\vec{\phi},c,T) + f_{orient}(\vec{\phi}) \right\} dV \qquad \textbf{Eq. 31}$$

where ϕ_i is an order parameter for a thermodynamic phase having a value of 1 in the solid

and 0 in the bulk liquid, $\vec{\phi}$ is an order parameter that describes misorientation between two solid

phases, $\varepsilon(\vec{\phi})$ is an anisotropic gradient free energy associated with misorientation between either

two solid-solid phases, or solid-liquid phases, $f(\vec{\phi},c,T)$ is the bulk free energy, and $f_{orient}(\vec{\phi})$ is

interaction energy between two solid phases of different orientations.

In the free energy above, the interplay between different phases, their concentrations and

the temperature of the solidifying system captures the interfacial, bulk and interaction

contributions to the free energy of a solidifying system.

Evolution of solidification microstructure can be described by solving the Cahn-Hilliard and

Allen-Cahn equations, given by:

$$\frac{\partial c}{\partial t} = \nabla \left(M(\vec{\varphi},c) \nabla \frac{\delta F}{\delta c} \right) \qquad \textbf{Eq. 32}$$

and

$$\frac{\partial \phi_i}{\partial t} = -K_\phi \frac{\delta F}{\delta \phi_i} \qquad \textbf{Eq. 33}$$

where $M(\vec{\varphi},c)$ is an interface mobility coefficient and K_ϕ is a kinetic coefficient that describes,

in a coarse-grained manner, atom attachment/detachment to and from a solid phase. The above

equations are variational in their formulation. However, in the model developed by Ofori-Opoku

et al., non-variational forms have been used to simulate dynamics. The reader is directed to the

source (Ofori-Opoku & Provatas, 2010) for the detailed formulation, but the key features of the

non-variational formulation will be discussed in this section.

The most important feature of the non-variational formulation is a modified diffusion equation (analogous to equation 33) that incorporates an *anti-trapping flux* term. This term accounts for solute trapping caused by employing a large diffuse interface. Use of an unrealistically large diffuse interface is justified since the scale of the diffuse interface is much smaller than the scale of the microstructure. Therefore the interface can be set at a reasonable value that makes numerical simulation possible. Therein lies the phase field method's core strength.

The simulated microstructures presented in this thesis are performed using a code developed by Greenwood (Greenwood, 2004) that implements an *adaptive gird/mesh*. An adaptive mesh is a non-uniform grid, which at any given time interval, adopts square elements of a large size where local variations are small and vice-versa. For e.g. local variations are small in bulk, but large at interfaces and grain boundaries. The adaptive mesh thus adds to the numerical efficiency allowing for microstructure on a large scale to be simulated. Examples of simulated microstructure are shown in Figure 11. The order and concentration maps are both shown for convenience. The order map shows variation of the order parameter across different phases. In the context of this thesis, there is only one such variation, which is from solid to liquid. The concentration map shows variation in solute concentration spatially, where the degree of hotness indicates the concentration of solute.
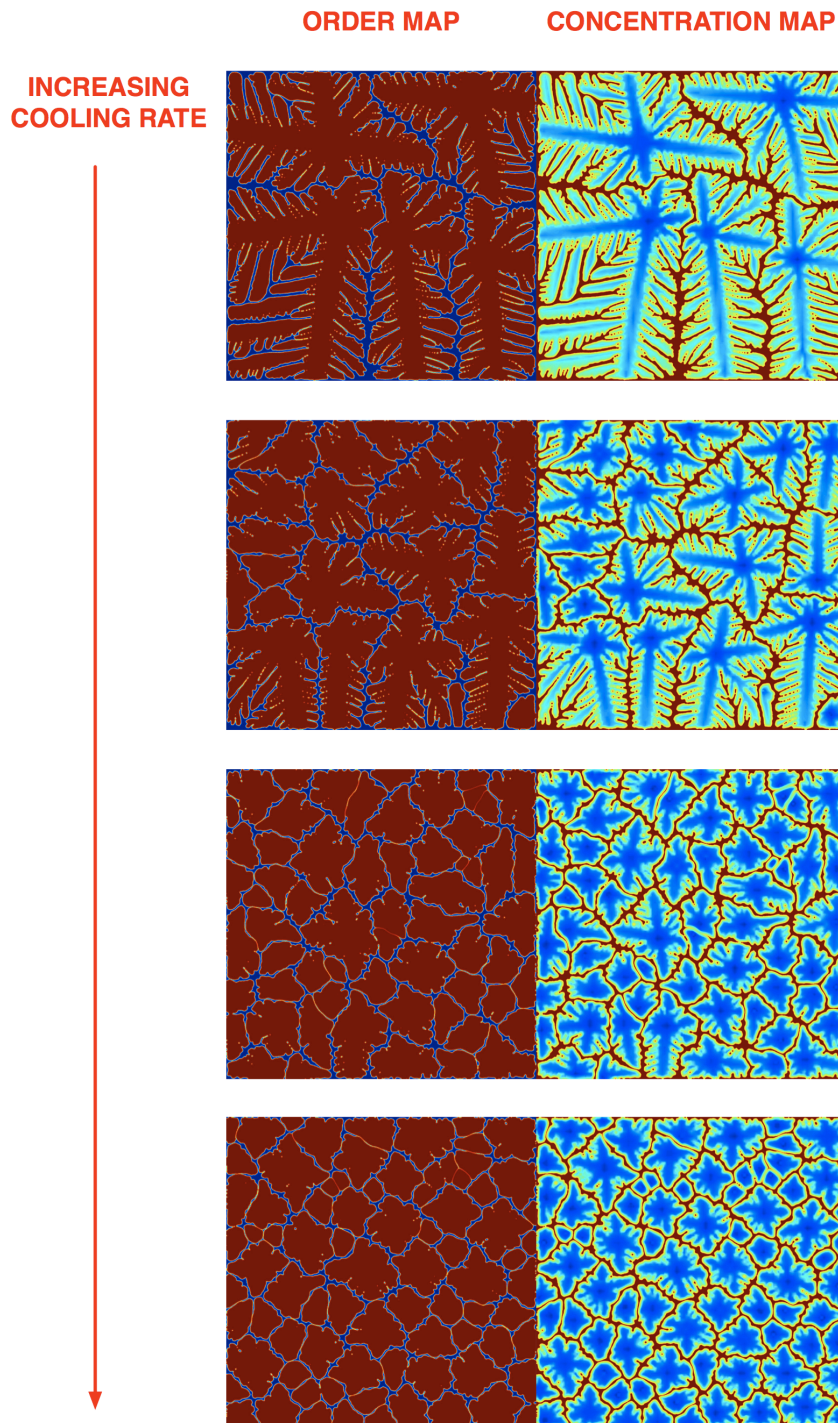
Figure 11–TYPICALEXAMPLESOFMICROSTRUCTURESIMULATAEDUSINGTHEPHASEFIELDMODEL

4.2 – NULCEATION AS IT PERTAINS TO THE PHASE FIELD MODEL

An important feature of equiaxed microstructure is the grain density, which is determined by the nucleation per unit volume (nucleation rate) and is directly correlated to late-stage liquid pooling. The intimate connection between grain density and nucleation rate is discussed below.

Nucleation as described in section 1.1.1 is also known as *thermal nucleation*. It is a suitable and realistic theory, but has some shortcomings. The nucleation rate is always expressed as a probability distribution that is a function of the number of sites(atoms/inoculants) in a system. Each atom/inoculant particle is a potential site for a cluster/nuclei to originate. This implies that upon sufficient lowering of temperature, every site is turned into a nucleus. This can mistakenly lead to the conclusion that the grain density for a system is a constant, which is contrary to observation (Figure 12).
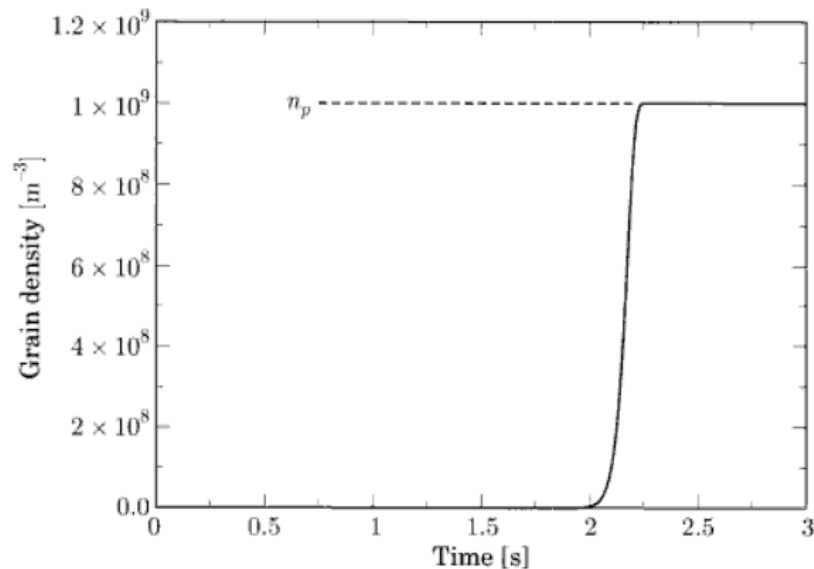

Figure 12 - GRAIN DENSITY VS. TIME AS PREDICTED BY HETEROGENEOUS NUCLEATION (Dantzig & Rappaz, 2009)

The grain density of a system is highly dependent on cooling rate, where a higher cooling rate, i.e. a higher undercooling, results in a higher grain density. The theory of *athermal*

nucleation, discussed below, takes into account the effect of cooling rate on the nucleation rate(Dantzig & Rappaz, 2009).

It can be pointed out at this juncture that the terms homogeneous and heterogeneous nucleation are identifiers for the *nucleation mode*, whereas the terms thermal and athermal nucleation describe the *temperature dependence* of the nucleation rate. In addition, it should be noted that homogeneous nucleation is always of the thermal kind, whereas heterogeneous nucleation can be either thermal or athermal. This is because for the case of homogenous nucleation every atom is a potential site, i.e. a cluster/nucleus can be arbitrarily centered on any atom.

In athermal nucleation the dependence of the nucleation rate on cooling rate is a result of the existence of a distribution of sizes of inoculants. The cooling rate determines the size range that is '*active*' and available for heterogeneous nucleation. All inoculant sizes may become active if the undercooling is large enough, and the nucleation process would then resemble the thermal kind. If the undercooling is not large enough, then there would exist a fraction of inoculants that do not become active. The fraction of inoculants that do become active would then be prescribed by the theory of athermal nucleation.

In the context of equiaxed solidification, there are two ways in which the inoculant size can limit the nucleation rate *at a given undercooling*.

- Case 1: The critical cluster size is bigger than all possible range of inoculant sizes (Figure 13).
- Case 2: The inoculant size permits formation of a cluster, but free growth is limited by the inoculant size. As can be seen in Figure 14, curvature needs to *increase* for further growth to occur.
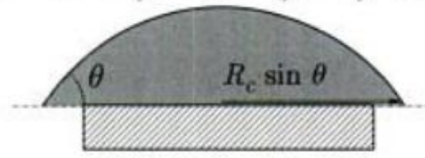
Figure 13 - CASE 1(Dantzig & Rappaz, 2009)
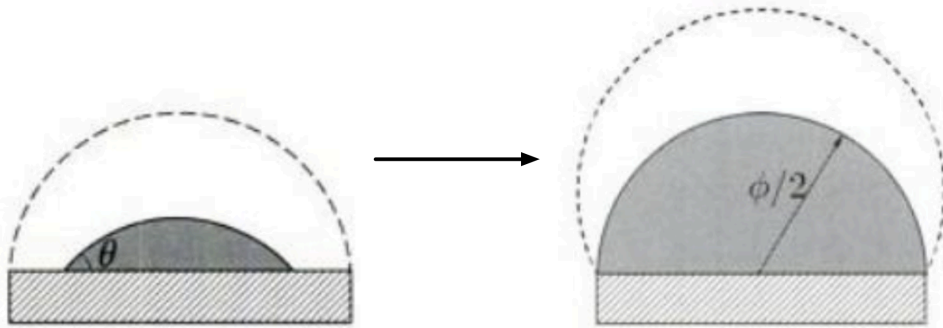
Figure 14 - CASE 2 (Dantzig & Rappaz, 2009)

Both these cases represent situations where all or some fraction of inoculants are not active. If the undercooling is kept constant, then the fraction of active inoculants is set, fixing the grain density in the system. For case 2, free growth (that minimizes curvature) is possible if the undercooling increases beyond the *geometrically limited undercooling*, defined as:

$$\Delta T_g = \frac{4\Gamma}{\theta}$$

<div align="right">Eq. 34</div>

where Γ is the Gibbs-Thomson coefficient (equation 18), and θ is the wetting angle between the substrate and the cluster/nucleus.
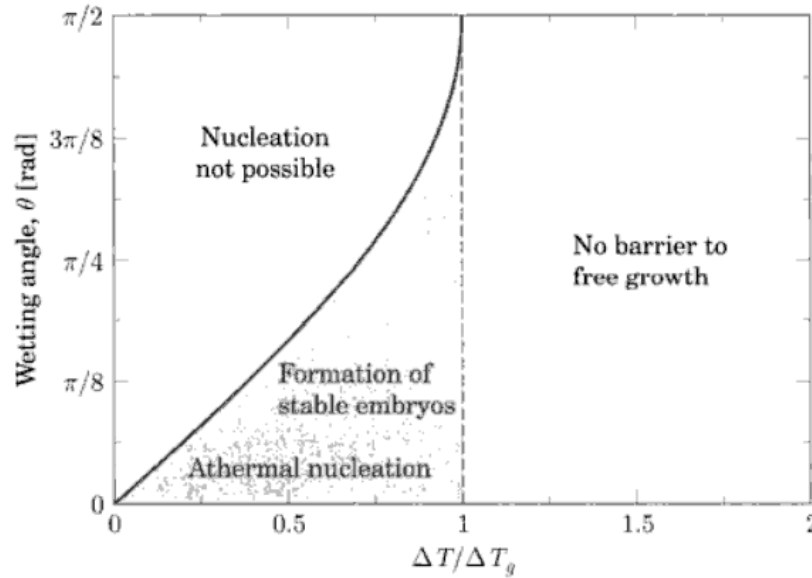
Figure 15 - EFFECT OF THE WETTING ANGLE ON THE EFFECTIVE UNDERCOOLING FOR NUCLEATION(Dantzig & Rappaz, 2009)

The size distribution of inoculants can be modeled in various ways, but was first done by Oldfield(Oldfield, 1966). Oldfield noticed that the grain density *N* was proportional to the square of the undercooling achieved. Mathematically this can be described as:

$$N = \eta \Delta T^2$$

<div align="right">**Eq. 35**</div>

where η is a fitting parameter. A size distribution in which regions are activated upon reaching a certain undercooling can be obtained by differentiating the above equation with respect to the undercooling:

$$\frac{dN}{d\Delta T} = 2\eta \Delta T$$

<div align="right">**Eq. 36**</div>

Note that the last two equations are similar to the ones comprising the nucleation and growth algorithm from the CA study highlighted in chapter 3.

A more realistic distribution comes from the observation that natural phenomena often display a lognormal behavior. Such a distribution can be formalized as follows:

$$\frac{dN}{d\Delta T} = \frac{N_{max}}{\sqrt{2\pi}\Delta T \Delta T_\sigma} \exp\left(-\frac{1}{2}\left(\frac{\ln \Delta T - \ln \Delta T_0}{\Delta T_\sigma}\right)\right)$$

Eq. 37

where N_{max} is the maximum number of inoculants in the system, ΔT is the inoculant size, ΔT_0 is the mean inoculant size, and ΔT_σ is the standard deviation.

Athermal nucleation can also appear due to existence of *different types of inoculants*, and is analogous to the size distribution effect. It serves to change the effective wetting angle θ, which in turn affects the geometrically limited undercooling ΔT_g.

In the context of the phase field modeling of microstructure, thermal fluctuations that drive nucleation are impractical to capture as they occur on incredibly short time scales and length scales below even that of the interface width. Therefore, a stochastic approach based on *effective nucleation probabilities* is employed (i.e. coarse grained to larger volumes and times)(Simmons, Shen, & Wang, 2000). It captures the effect of cooling rate on grain density, and is discussed below.

The nucleation rate was identified in section 1.1.1 as:

$$\dot{N} = Z\beta N_l \exp\left(-\frac{\Delta G_{nuc}}{k_B T}\right)$$

Eq. 38

where β is the attachment frequency, Z is the Zeldovich Factor, N_l is the total number of atoms in the system, G_{nuc}^* is the 'activation energy' of nucleation.

On an adaptive mesh, each element is arbitrarily defined as a test volume where nucleation can occur based on a probability $P_{\Delta v, \Delta t}$ over that volume and in one numerical time step. Nucleation in an element Δv occurs if the probability of nucleation, a function of the

nucleation rate $\dot{N}$, is greater than a number between 0 and 1, chosen from uniform random distribution by a random number generator at each element at every time step. When this occurs, a circular grain of size sufficiently greater than the critical radius is placed at a seed within the element. The seed is then 'burned", which means that it is no longer available as a nucleation site.

The probability of nucleation in an element Δv is obtained as:

$$P_{\Delta v, \Delta t} = 1 - \exp(-\dot{N} \Delta v \Delta t) \qquad \qquad \textbf{Eq. 39}$$

where Δt is a time interval chosen to be large enough to capture the spatial compositional fluctuations (noise) responsible for at most one nucleation event in the time window $(t, t + \Delta t)$.

Referring back to Equation 39, for a constant temperature window, the size of the time window in which nucleation events occur is inversely proportional to the cooling rate. Therefore, for low cooling rates a larger time window will allow seeds that nucleate on the onset to grow and hinder nucleation of other seeds at a later time. This hindrance is due to solute segregation and a decrease in the ratio of liquid-to-solid volumes. This does not occur for sufficiently high cooling rates, where the time window for nucleation is so small that nucleation events do not interfere with each other. As a result most/all active sites nucleate. Consequently, a higher grain density for high cooling rates is observed compared to low cooling rates. Microstructures for various cooling rates are shown in Figure 11.

4.3 – SPECTRAL ANALYSIS: DIRECTIONAL VS. EQUIAXED SOLIDIFICATION

The phase field model described above and the theories that constrain and shape its behavior only serve to produce quantitatively accurate microstructure. Therefore, in the context of this thesis, it is but a tool to produce such microstructure. Consequently, prominence is given to analytical techniques that can be used to elucidate and quantify trends and patterns within this

microstructure. Accordingly, results presented and discussed in chapter 5 of this thesis are a product of the analytical techniques presented in this section and the next.

Spectral analysis has been an invaluable tool for making sense of an apparently stochastic process to draw out patterns and periodicities. It has wide variety of applications, from the analysis of light from stars to electrical signals, In essence, discrete spectral analysis consists of sorting data into bins where the 'weight' of each bin indicates the prevalence of a given frequency of oscillation of signal. This is appreciated when it is realized that all continuous (or piece-wise continuous) signals can be decomposed into a series of sine waves.

Examples of power spectra of three different signals are shown in Figure 16. The green wave is a linear combination of the red and the blue waves. Its power spectrum has two peaks, which tells of two predominant wavelengths. The frequencies of the two predominant wavelengths are indicated on the x-axis, and the amplitude on the y-axis indicates equal significance/contributions from the two predominant wavelengths.
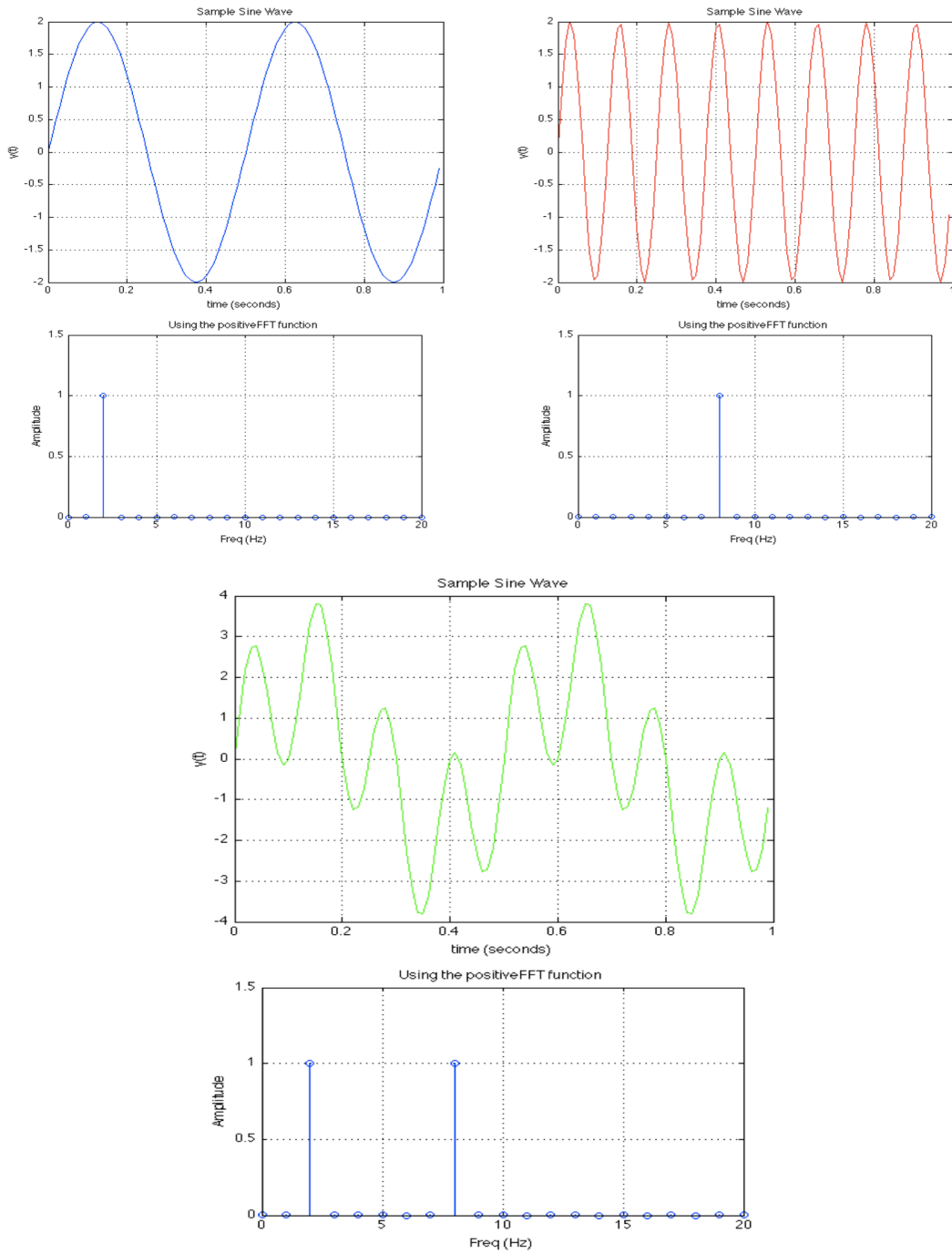
Figure 16 - EXAMPLES OF POWER SPECTRA OF VARIOUS WAVES

The idea presented above is formalized using a Fourier Transform for a continuous analytic function or a Discrete Fourier Transform (DFT) for discretely sampled date. The one-dimensional DFT of a set of data $\{f_n\}$ representing samples of a function $f(x)$ is given by:

$$F_k = \frac{1}{\sqrt{N}} \sum_{n=0}^{N-1} f_n e^{2\pi i n k / N}$$ **Eq. 40**

where k is the wavenumber index and F_k is in general complex. The *one-dimensional* (1D) power spectrum is defined as the real-valued squared amplitude of the Fourier Transform:

$$\left| F(k) \right|^2$$ **Eq. 41**

For the analysis of two-dimensional (2D) data, one needs the 2D Fourier Transform. A convenient tool for analysis of 2D data is the radially averaged power spectrum, which can be defined as:

$$S(k) = \left\langle \left| F(\vec{k}) \right|^2 \right\rangle_{rad}$$ **Eq. 42**

where the brackets indicate radial averaging in reciprocal space over values of k of equal magnitude. In other words, a 2d data set is binned into predominant inverse wavelengths (i.e. frequencies) along the x and y directions, also known as wavevectors, and then circularly averaged about the origin. An example of such a 2d data set is a picture of microstructure produced from phase-field simulations (to be discussed in the next chapter), shown in Figure 17 along with its radially averaged 2d power spectrum.
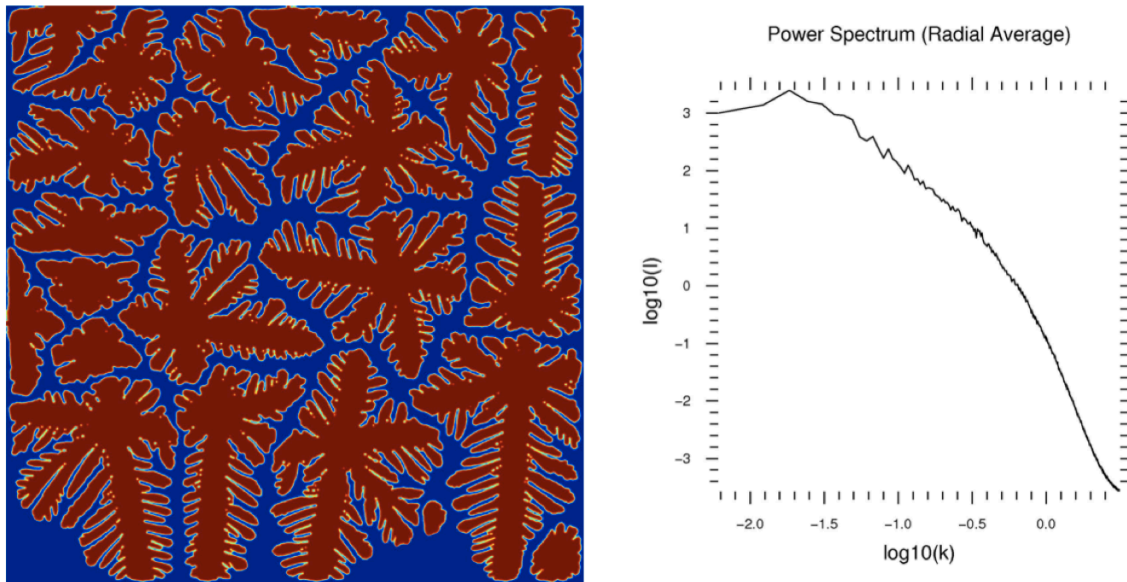
Figure 17 - POWER SPECTRA FROM MICROSTRUCTURE

Spectral analysis has also been successfully used to elucidate length scale selection in other contexts. In the case of directional solidification, it was used by Greenwood et. al and Amoorezaei et al.(Amoorezaei, Gurevich, & Provatas, 2010; Greenwood, 2004; Gurevich et al., 2010) to identify mean primary dendrite spacing. Results from Amoorezaei et al. are shown in Figure 18. Here, the mean peak of the power spectra is proportional to the inverse of the primary dendrite spacing.

Figure 18 - POWER SPECTRA RESULTS FOR PRIMARY DENDRITE ARM SPACING(Amoorezaei, 2012)
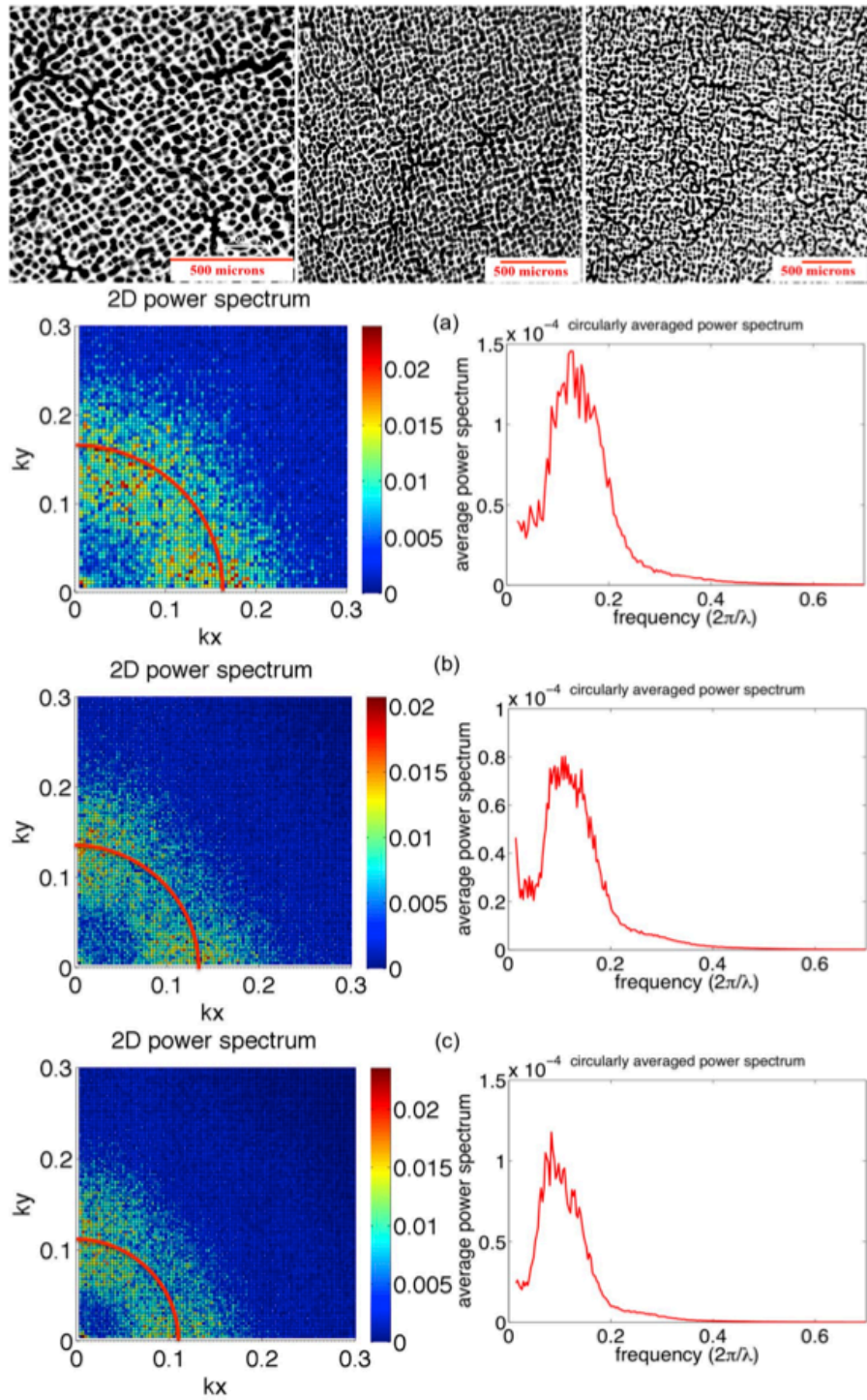
Returning to the case of equiaxed solidification, the radially averaged 2d power spectrum identifies a variety of features/lengthscales. Figure 17 is presented again with these features identified in Figure 19. Here, smaller features are represented at large k values on the x-axis, with their relative amounts given by the intensity values on the y-axis.
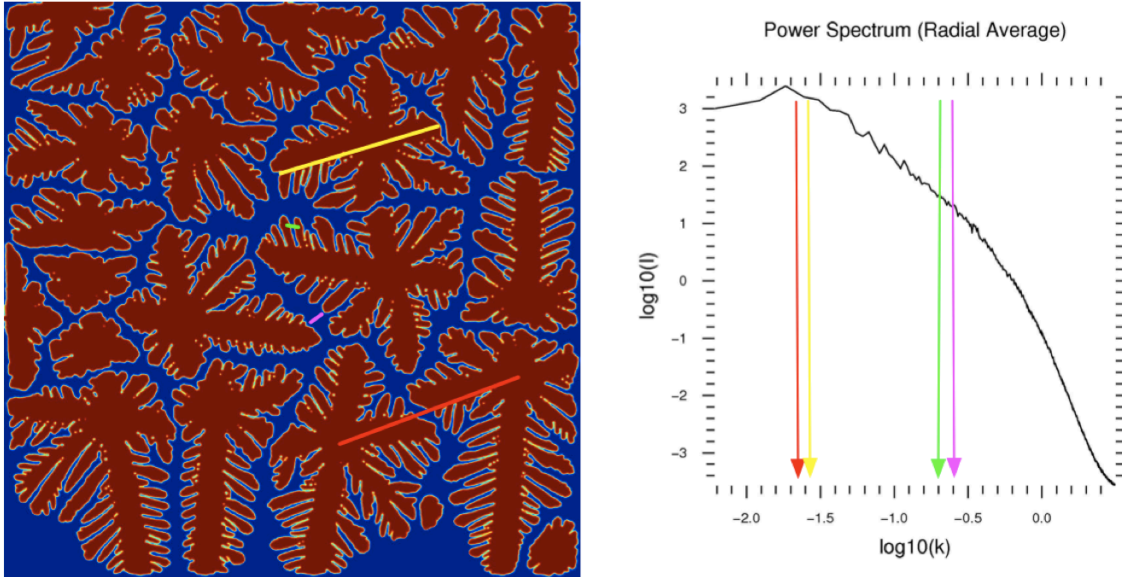

Figure 19 - POWER SPECTRA FROM MICROSTUCTURE WITH FEATURES

Note that the liquid pool structure can be identified visually, but is not obvious in the power spectrum. In the case of directional solidification, the feature of interest (primary arm spacing) was obvious as a well-defined peak. In the case shown here, there is a weak peak corresponding to the inter-grain spacing. However, the more interesting feature is the self-affine scaling that exists through some length scales of the liquid pool. The power law in the spectrum in the figure above evidences this. The power spectrum in the high wavenumber region, i.e. where the interfaces (as opposed to the dendritic structure) become the predominant feature in the system, is expected to conform to Porod's Law, which states the following power law behavior (in 2D):

$$S(k) \sim k^{-4}$$

<div style="text-align:right">**Eq. 43**</div>

In the case of equiaxed structures, power spectral analysis is inadequate, alone, to highlight liquid pool evolution. This is further discussed in section 5.1, where results from simulations representing various cooling rates are discussed.

4.4 – CLUSTERING ANALYSIS

As briefly noted in the previous section, spectral analysis as a tool for the analysis of liquid pool evolution has some limitations. Therefore an additional technique is required that can highlight various aspects of late-stage liquid pools.

To that aid, the method of *clustering analysis* is employed. For a given data set, a *clustering algorithm* groups together data points that are similar to each other. The similarity criterion is often prescribed based on the nature of the application, and usually requires a tolerance to be specified by the user of the clustering algorithm. This tolerance sets a limit on how different two data points can be with respect to each other before they are considered to belong to two different groups.

Clustering algorithms are notoriously prevalent in our daily lives. One example of a clustering algorithm is of the kind that recommends books on Amazon.com, the online retailer. When a particular search query is made, a clustering algorithm is usually at work that organizes the entire amazon.ca library into two groups of data: one that contains books matching the search query, and one where books do not match the search query.

Analogously, clustering analysis applied to simulated microstructural data such as one shown in Figure 17groups together data points that are liquid (blue), and data points that are solid (red). Therefore it identifies individual liquid pools. The clustering algorithm applied here also counts and tracks the size of individual liquid pools, effectively tracking liquid pool evolution.

In the context of this thesis, the clustering algorithm used is known as the *Hoshen-Kopleman* algorithm(Fricke, 2004). It is visually depicted in Figure 20.

Figure 20 - HOSHEN-KOPLEMAN ALGORITHM(Fricke, 2004)

For the case of a data set such as a 2d binary matrix, a *cell* (data point) is considered occupied if it contains a '1', and is considered unoccupied otherwise. The Hoshen-Kopleman algorithm scans the matrix for occupied cells, and determines their connectivity by looking at any occupied neighbors. The matrix is actively re-labeled as the algorithm scans it, with each unique label indicating a cluster. The value of the maximum label gives the number of clusters in the system, and the amount of labels in any given cluster indicated its size. In other words, when applied to microstructure data, the number and the size of liquid pools in the system are obtained. The result of the clustering algorithm when applied to simulated microstructure is shown in Figure 21, where each color in the right thumbnail represents a cluster.
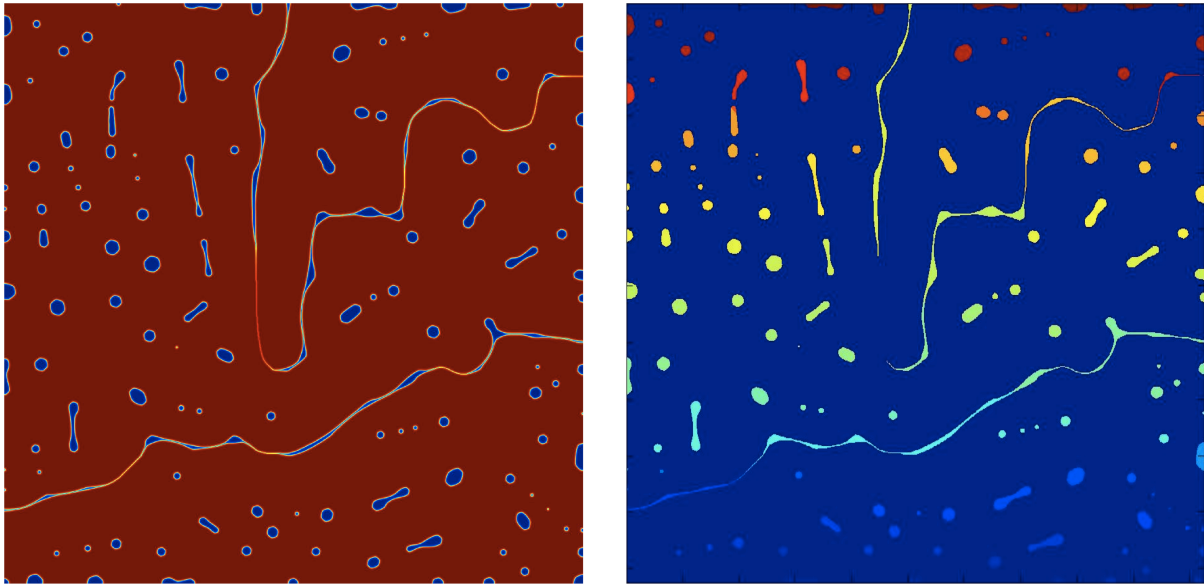
Figure 21 - HOSHEN KOPLEMAN ALGORITHM APPLIED TO MICROSTRUCTURE

CHAPTER 5 – REULTS & DISCUSSION

In this chapter, the effect of cooling rates and solid diffusion coefficient (back-diffusion) on liquid pool evolution is investigated using the methods presented in chapter 4. Specifically, spectral analysis is used to highlight the effect of cooling rate, while clustering analysis and the subsequent percolation methods are used to highlight the effect of cooling rate *and* solid diffusion coefficient.

5.1 – SPECTRAL ANALYSIS OF LATE-STAGE LIQUID POOLS

Figure 19 in section 4.1.4 highlights a typical power spectrum with marked features. In time, the marked features shift on the power spectrum, and the displacement in either the left or the right direction indicates feature evolution from a small to big length scale or vice-versa. The average center-to-center grain distance (red marker) doesn't change in time, since the position of grains is set once nucleated. The average grain size (yellow marker) shows a slight shift towards the left as it increases over time. The secondary arm spacing (green marker) also shows this behavior, since secondary arms coarsen over time. The liquid pool width (purple marker) shows displacement towards the right on the power spectrum, as it shrinks and disappears as grains merge.

Another notable characteristic of the power spectrum over time is the decrease in the intensity, shown in Figure 22. This is due to the coarsening and disappearance of structure over time. As the microstructure becomes increasingly homogenous, the only distinguishable peak corresponds to the average grain size.
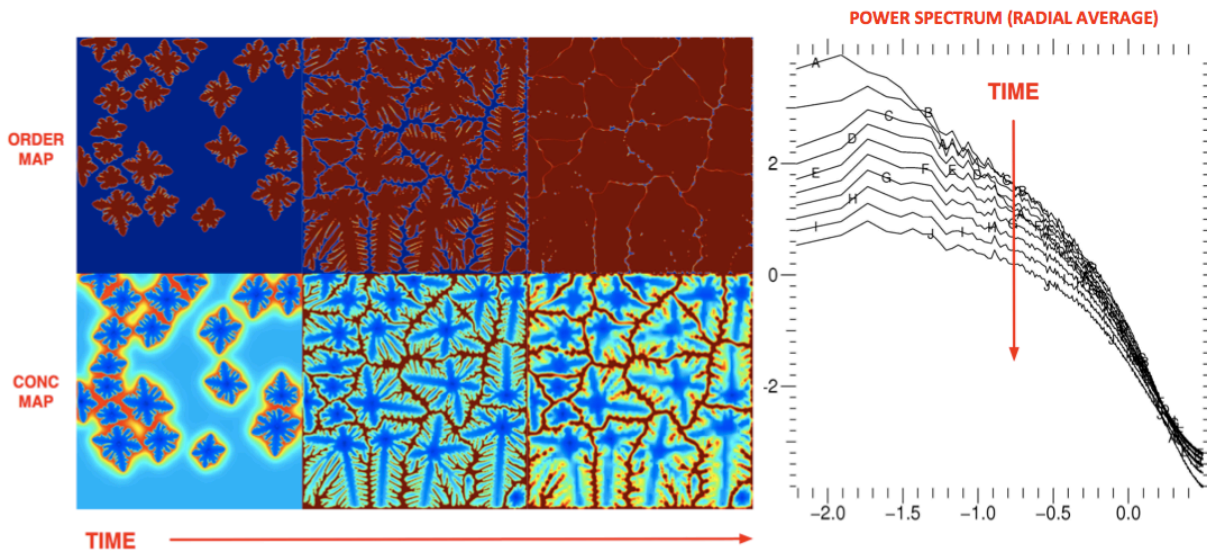
Figure 22 - Evolution of the Power Spectrum over time for a given system. The term 'conc' represents concentration in the figure.

It was also argued in the section 4.1.4 that power spectral analysis is inadequate, alone, to elucidate liquid pool evolution due to lack of any obvious corresponding peak. However, there is one feature of the power spectrum that elucidates the structure of the liquid pools. This feature is the region of linearity (in a log-log plot) associated with all wavelengths that are of relevance within the system. This is shown in Figure 23. At best, the right and left extremes of this linear region indicate the liquid pool colony size and potential liquid pool colony spacing, where a liquid pool colony is an isolated interconnected liquid pool. Alternatively, the right and left extremes tell of the smallest and the biggest features in the microstructure of the system. In this context, the smallest features are the spaces between secondary arms and the biggest features are the grains.
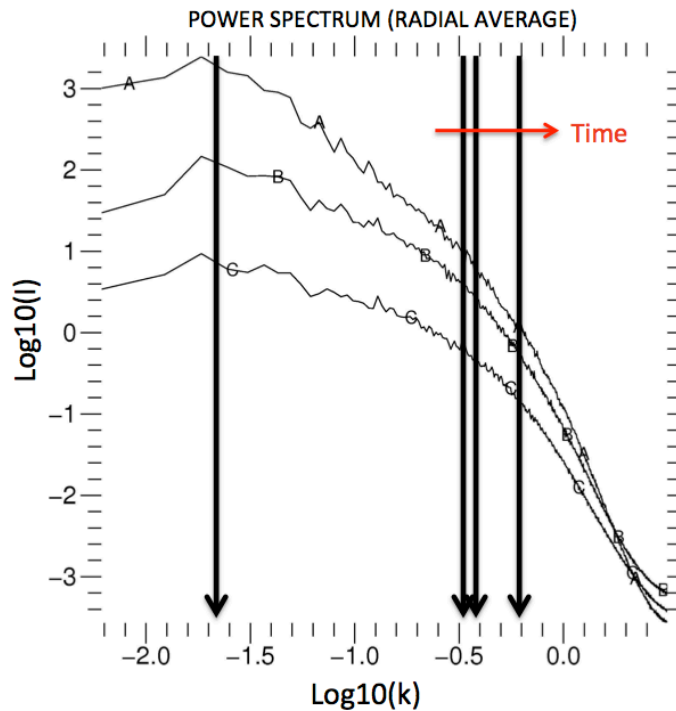
Figure 23 - Power spectrum with region of linearity indicated

A shortcoming of such an analysis is the arbitrary nature of the linear region, i.e. there is no unambiguous way to determine the left and right extremes. This was also the case in(Gurevich et al., 2012). It must be noted that despite the approximate nature of the linear region, its implications are quite clear.

A linear region is indicative of a power law that maps onto self-affine features existing within a system, where the slope of the linear region is related to the evolution kinetics. A classic example of a self-affine morphology is a dendrite. Therefore in this context, the linear region indicates the kinetics of evolution of dendritic features that coarsen over time. The decreasing slope and extent of this linear region in time tells of decreasing mobilities of diffusional species associated with coarsening, and physically manifests in a lowering of the number of dendritic features and their coarsening rate.

Power spectra for three cooling rates are highlighted in Figure 24. These have been averaged over 10 simulations for each cooling rate. A Gaussian filter was applied to smooth out any rough features. There is a definitive shift of the main peak downward and to the right of the power spectra, indicating the presence of smaller grain sizes.
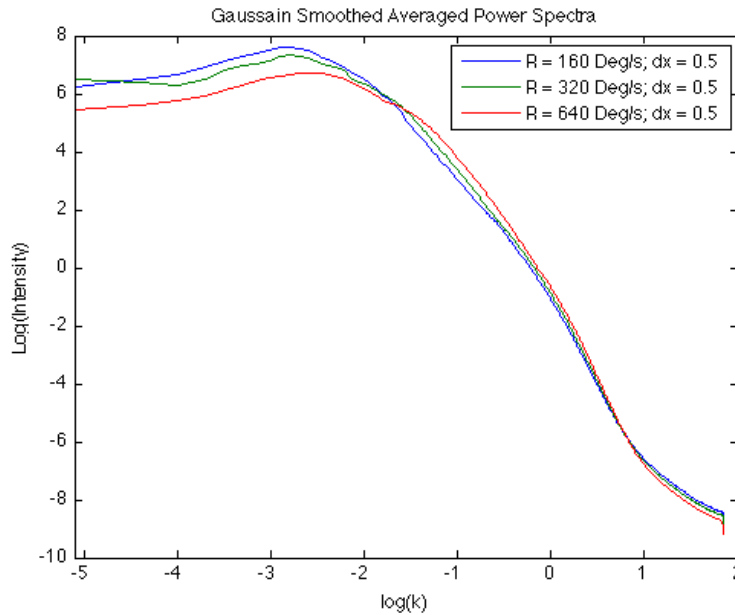

Figure 24 - Power Spectra for varying cooling rates

5.2 –CLUSTERING ANALYSIS OF LATE-STAGE LIQUID POOLS

An adequate scheme of presenting the results from the application of the Hoshen-Kopleman clustering algorithm (described in section 4.4) is the variation in number of liquid pools vs. liquid fraction in the system. Figure 25shows one such typical result. Solidification proceeds from right to left along the curve, and some snapshots of microstructural evolution are shown alongside for convenience.
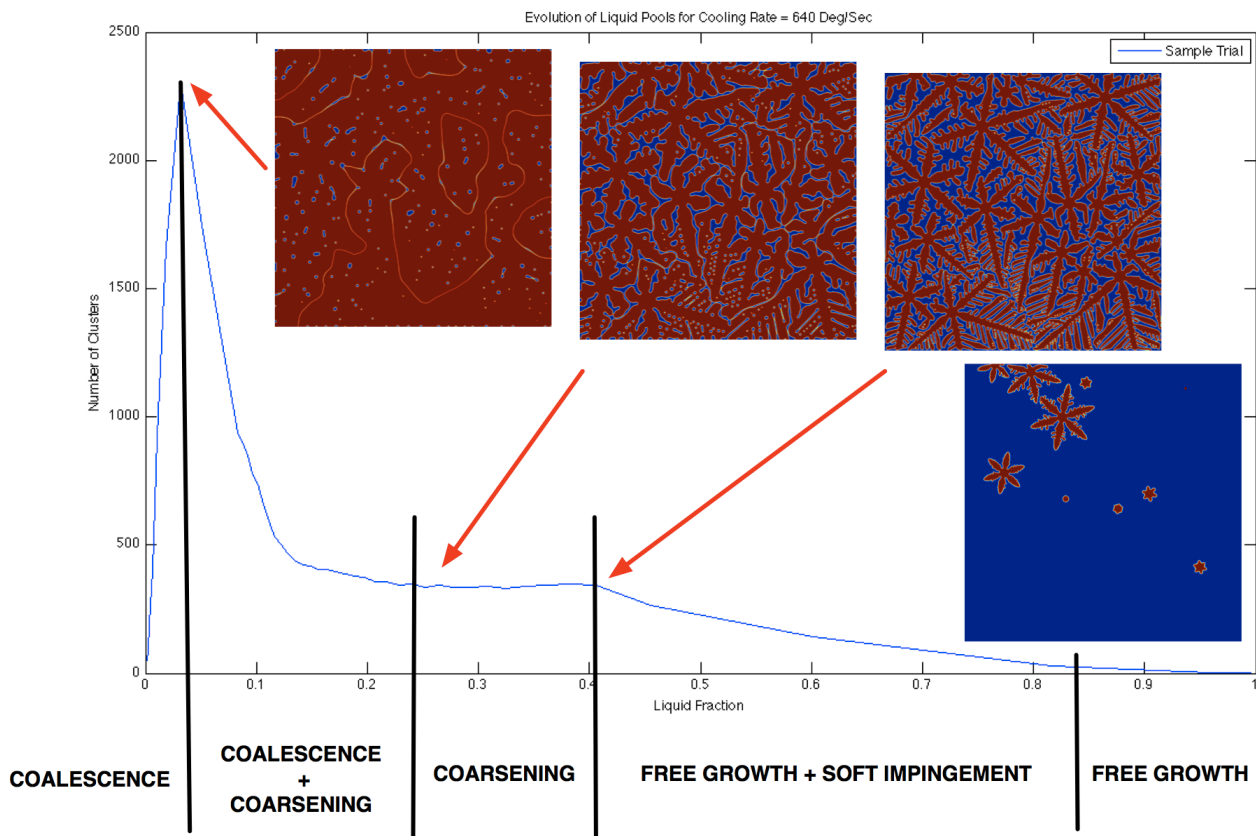
Figure 25 - Typical example of Evolution of Liquid Pools obtained from the Hoshen-Kopleman clustering algorithm

As with all results presented in this section, this plot was obtained by averaging ten simulation trials at the same cooling rate, but different initial conditions by way of random nucleation.

This typical number vs. liquid fraction curve exhibits two maxima and one minimum, highlighted by the red arrows. The first maximum corresponds to the point where nucleation stops occurring, i.e. the point at which nucleation rate has decreased to zero. The increase in the number of clusters is due to entrapment of liquid pools between secondary arms. The large average size is due to the contribution of large networks of liquid pools, where each network is considered a cluster. The following decrease in the number (and also average size of clusters,

seen, for e.g., in Figure 28)corresponds to the onset of soft impingement processes that lead to merger of secondary arms and decrease of width of networked liquid pools. The minimum corresponds to the onset of coalescence whereby the existing liquid pools networks are pinched off to form isolated liquid pools. This leads to a sharp increase in the number of liquid pools (and also a rapid decline in their average size seen, for e.g., in Figure 28). The second maximum corresponds to the point where mostly coalescence processes are in operation. This leads to rapid closure of liquid pools and consequently a rapid decline in their numbers.

Using the Hoshen-Kopleman clustering algorithm, evolution of liquid pools with respect to varying *cooling rates* and *solid diffusion coefficients* was investigated. The results are shown and discussed in the following sub-sections.

5.2.1 – EFFECT OF COOLING RATE ON LIQUID POOL EVOLUTION

The trend described in the preceding section is shown across various cooling rates, which are shown in Figure 26. An increase in cooling rate leads to a higher overall number of clusters of smaller sizes, consistent with experimental observations of large number of smaller sized second phases with an increase of cooling rate(Sarreal & Abbaschian, 1986). The apparent contraction of the curve in the horizontal direction can also be attributed to the cooling rate, where the sizes of liquid pools formed are constrained by the increased number of nuclei/grains in the system.
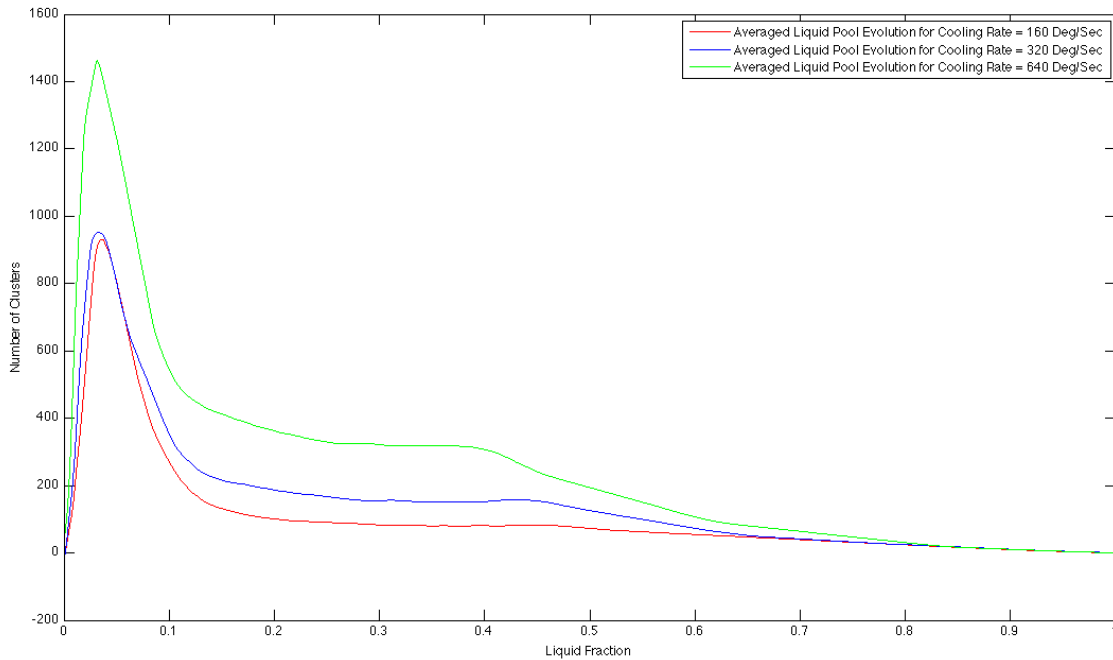
Figure 26 - Evolution of Liquid Pools(Number of Liquid Pools vs. Liquid Fraction)for varying cooling rates

The evolution of the number of clusters can be tracked with respect to other variables, notably *temperature* and *average pool size*. The shape of the curve remains relatively the same, along with the features and trends described earlier for the number vs. liquid fraction plot. These plots for various cooling rates are shown in Figure 27 and Figure 28. For the case of number of pools vs. average size, a close up of the region where most of the liquid pool evolution occurs is shown.
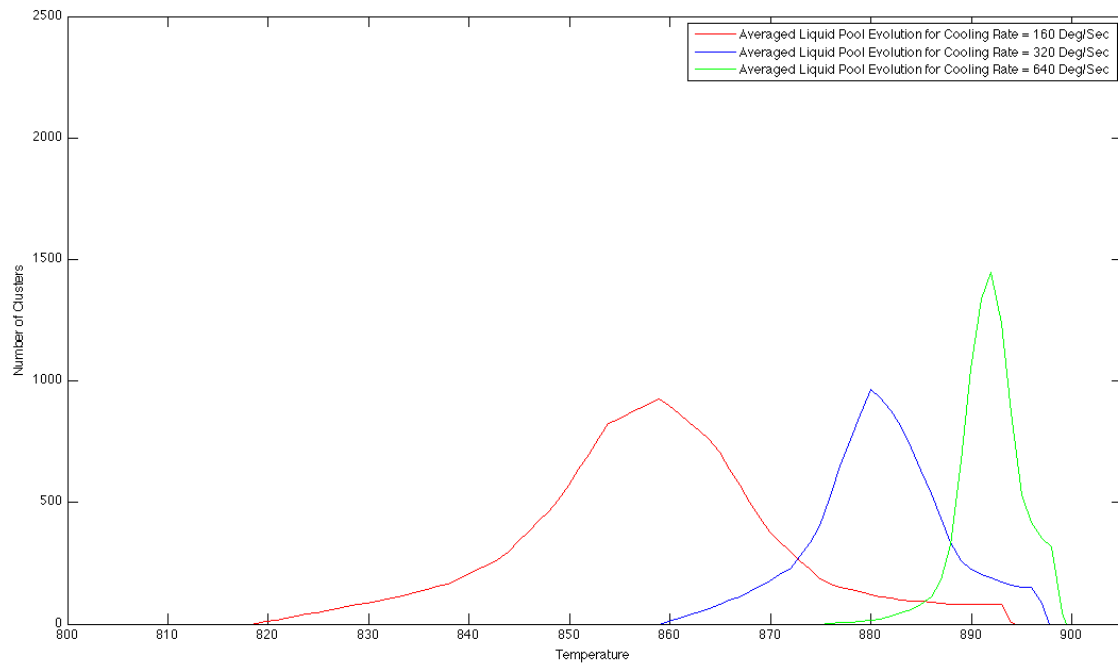
Figure 27 - Evolution of Liquid Pools (Number of Liquid Pools vs. Temperature) for varying cooling rates

Figure 28 - Evolution of Liquid Pools (Number of Liquid Pools vs. Average Size) for varying cooling rates

5.2.2 – EFFECT OF SOLID DIFFUSION COEFFICIENT ON LIQUID POOL EVOLUTION

Another effect that was investigated was with respect to the diffusion coefficient in the solid. Three diffusion coefficients were investigated. Plots similar to Figure 26, Figure 27 and Figure 28 were produced and are shown in Figure 29, Figure 30 and Figure 31.

Figure 29 - Evolution of Liquid Pools (Number of Liquid Pools vs. Liquid Fraction) for varying solid diffusion coefficients

Figure 30 - Evolution of Liquid Pools (Number of Liquid Pools vs. Temperature) for varying solid diffusion coefficients

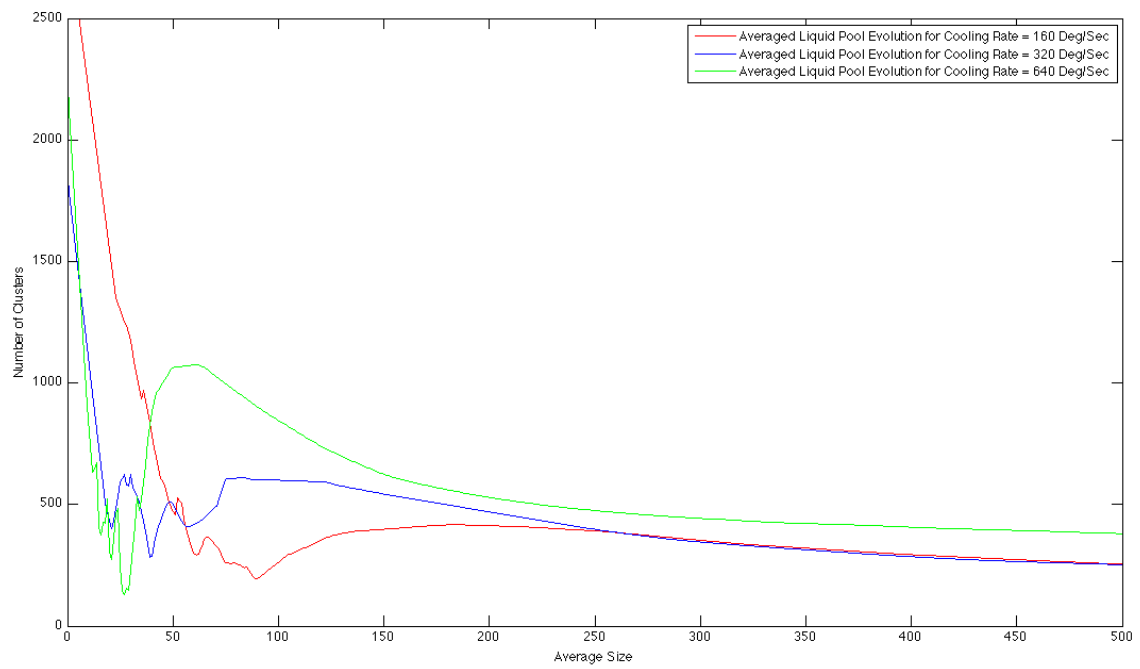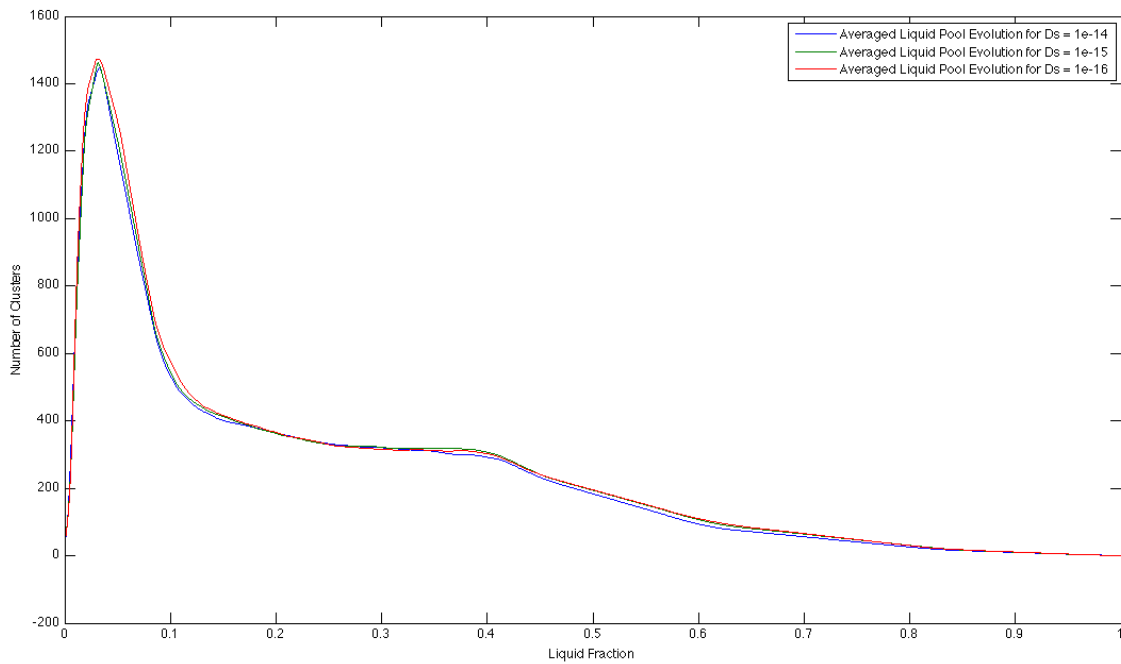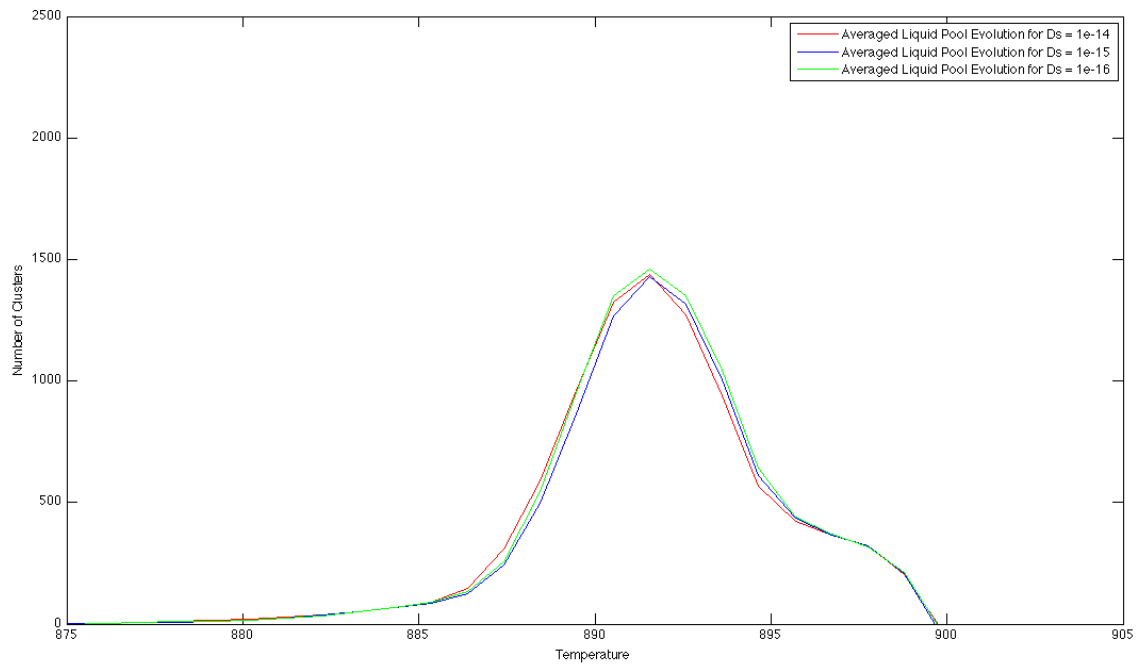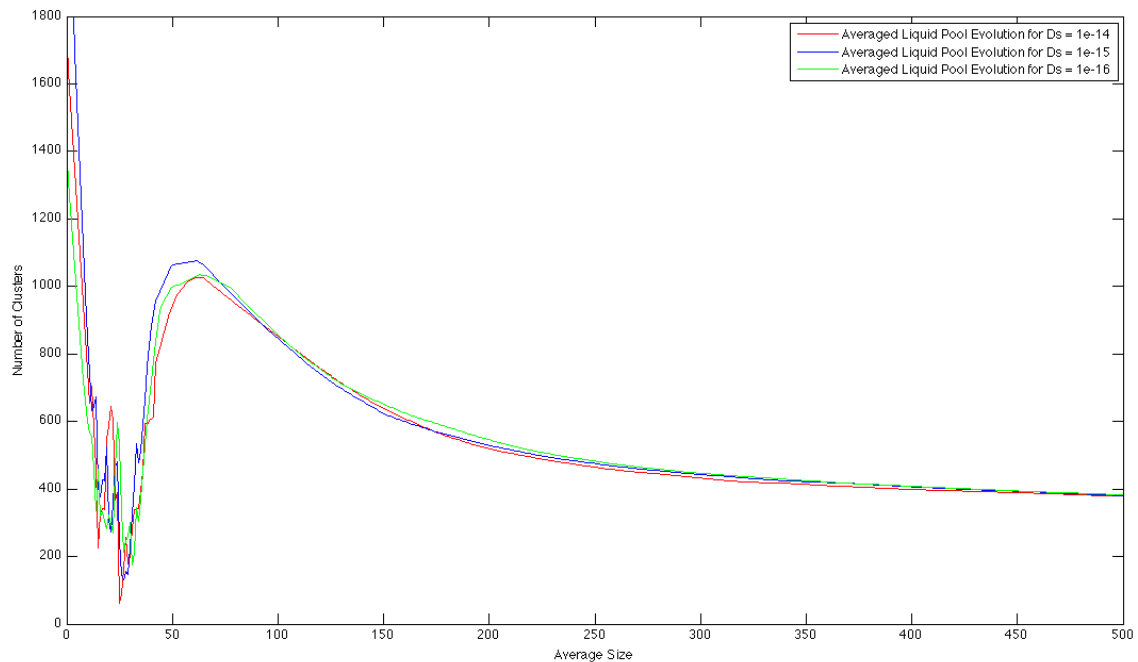**Figure 31 - Evolution of Liquid Pools (Number of Liquid Pools vs. Average Size) for varying solid diffusion coefficients**

Figure 29 through Figure 31 show an almost negligible difference with varying solid diffusion coefficients. However, it will be discussed shortly that this difference can be drawn out and expanded upon.

5.2.3 – COMMENTS ON RESULTS OF CLUSTERING ALGORITHM

It can be pointed out at this juncture that the similar shapes and features of each of the three types of plots elucidates the coupled nature of the number of liquid pools, their sizes, liquid fraction and temperature. In other words, they are not independent of each other. It should also be noted that the number of liquid pools times the average size equals liquid fraction. Thus, it is possible to determine the amount of liquid pools from a number vs. size plot, and the size of the liquid pools from a number vs. liquid fraction plot.

The type of plot that is arguably the most adequate scheme to highlight further analysis is of the number vs. liquid fraction type. This is because unlike temperature or average size, the values of liquid fraction are bounded. That is, it does not discriminate between solidification processes occurring in very different systems (for e.g. different alloys, compositions, freezing ranges, etc.) and displays any prevailing trends in a pseudo-'*normalized*' fashion. The region of interest with regards to the distribution of second phases within such plots is arguably between the first maximum and the minimum. This is because the distribution of liquid pools within this region is very similar to the distribution of second phases as seen from literature (Czerwinski, 2011). In addition, it can be argued that the chances for second phase formation are reduced upon onset of coalescence processes. Coalescence is accompanied by back-diffusion, which reduces the solute content within liquid pool, which in turn may be required to nucleate a second phase. Additionally, coarsening also implies a reduction in the available liquid for nucleation of a second phase, which in turn may decrease the final amount of second phases.

5.3– APPLICATION OF PERCOLATION METHODS TO CLUSTERING ANALYSIS

Bringing the work of Brunini et al. (Brunini et al., 2011) back into focus, liquid pool evolution for equiaxed solidification can also be analyzed as a percolating network. The number of liquid clusters vs. liquid fraction plot can be extended to the kind seen in Figure 9, where probability of having a spanning cluster is plotted vs. liquid fraction. For the analysis presented subsequently, each set of data has been averaged over 10 simulations. These plots, shown and discussed in the following sub-sections, are relatively rough despite being averaged over ten simulations. The address this, the rough averaged data was fitted with a function of the form of a cumulative probability for a normal distribution. The fitting function is of the form:

$$P(S) = \frac{1}{2}\left[1 + erf\left(w\left(f_l - f_l^{avg}\right)\right)\right]$$

Eq. 44

where $P(S)$ is the probability of finding a spanning cluster at a liquid fraction f_l, f_l^{avg} is the average liquid fraction threshold/average percolation threshold, and w is the width of the percolation transition. The trends exhibited by the fitting error functions can be viewed as the variation of two parameters: f_l^{avg} and w, where they are responsible for horizontal shifts and broadening/sharpening respectively. These parameters connect with Figure 26 and Figure 29by way of w mapping on to the distance between the first maximum and the minimum, and f_l^{avg} corresponding to its midpoint. The values for these two parameters for the cases of different cooling rates and diffusion coefficients are given in Table 1.

Table 1 - Fitting parameters for application of percolation methods to clustering analysis

Cooling Rate ($\dot{R}$)			Solid Diffusion Coefficient (D_s)		
	w	f_l^{avg}		w	f_l^{avg}
$160 ^\circ C / s$	20	0.38	$1e-14$	25	0.35
$320 ^\circ C / s$	27	0.36	$1e-15$	35	0.35
$640 ^\circ C / s$	33	0.345	$1e-16$	45	0.35

5.3.1 – PERCOLATION METHODS RESULTS FOR VARYING SOLIDDIFFUSION COEEFICIENT
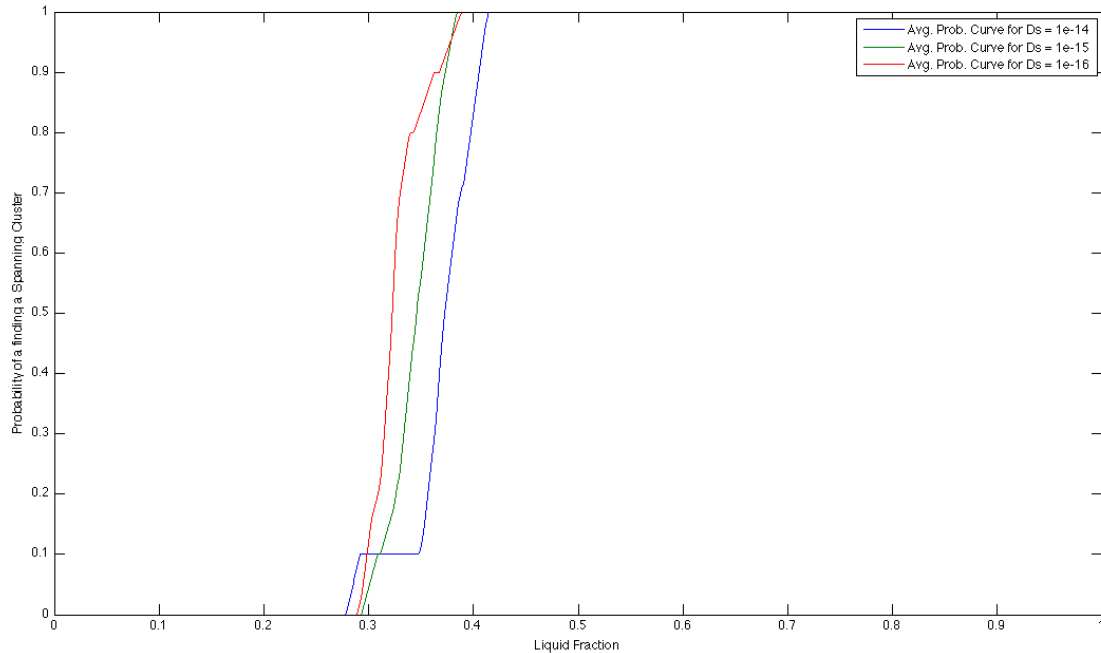

Figure 32 – Probability of having a Spanning Cluster vs. Liquid Fraction for varying solid diffusion coefficients

Figure 32 and Figure 33 show the raw and fitted spanning cluster vs. liquid fraction plots for the case of varying solid diffusion coefficients, the only observable trend in the data is a slight sharpening of the error function fit with an increase in solid diffusion coefficient. This implies that for a higher solid diffusion coefficient, the percolation transition starts at a lower liquid fraction and leads to a slower pinch off of liquid pool networks to form isolated pools. This is facilitated by the faster rate of back-diffusion, which reduces the curvature of approaching interfaces, and delays coalescence processes (Ofori-Opoku & Provatas, 2010; Rappaz et al., 2003). Another feature of the fits for this case is that the error function fits have a common intersection point at $P(S) = 0.5$ and $f_l = 0.35$, which suggests that at these values the liquid pool structure is statistically the same.
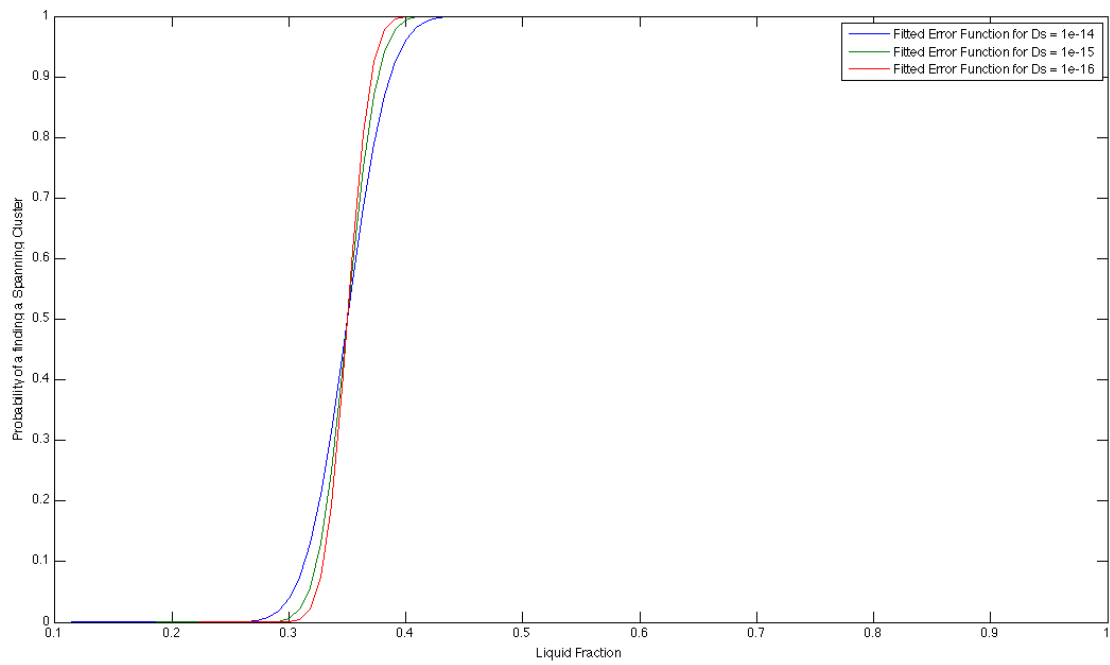
Figure 33 – Probability of having a Spanning Cluster vs. Liquid Fraction for varying solid diffusion coefficients fitted to equation 44 using parameters given in Table 1

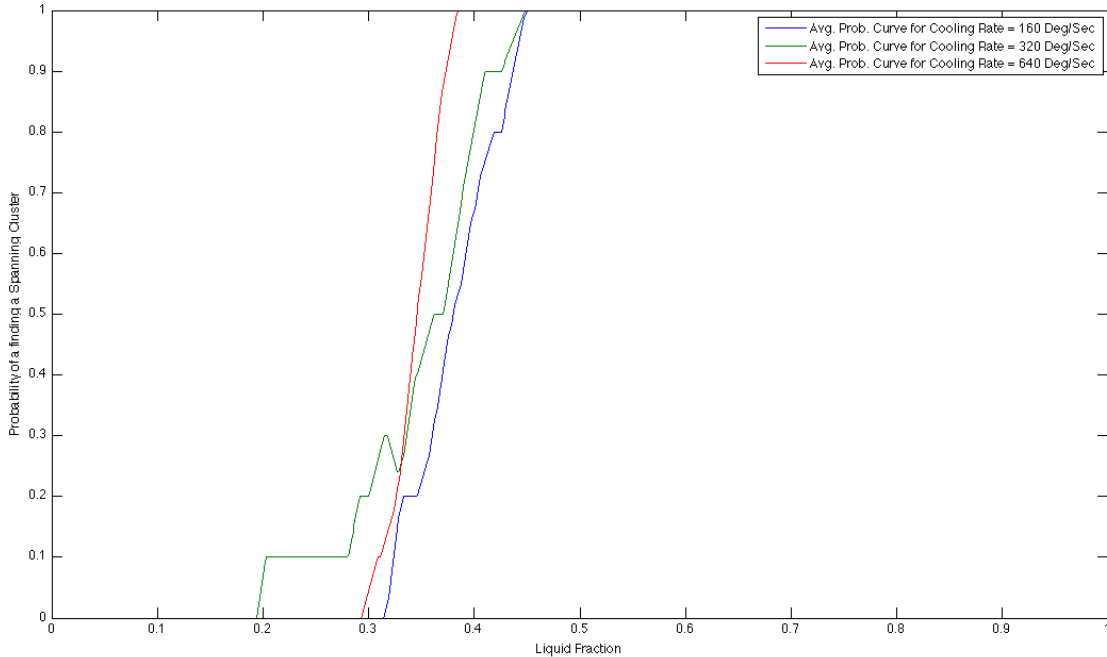*5.3.2 – PERCOLATION METHODS RESULTS FOR VARYING COOLING RATES*

Figure 34 - Probability of having a Spanning Cluster vs. Liquid Fraction for cooling rates

Figure 34 and Figure 35 show the raw and fitted spanning cluster vs. liquid fraction plots for the case of varying cooling rates. In this case, the observable trends are more complex. There is a sharpening of the error function fit *along* with a horizontal shift towards lower values of liquid fraction with an increase in cooling rate. The sharpening of the error function fit has the same implications as described for the varying diffusion coefficients case. The horizontal shift implies that the percolation transition occurs at a lower liquid fraction, but does not lead to a faster pinch off. The combination of the error function sharpening and horizontal shift with increasing cooling rates leads to a percolation transition at a lower liquid fraction *and* leads to faster pinch off. This in turn leads a large number of small sized liquid pools in the system.

Another way of interpreting the error function fits is to observe the corresponding number of liquid pools vs. liquid fraction plot, shown in Figure 26. There is a pronounced shift of the first

maximum towards lower liquid fraction as the cooling rate increases. The minimum however, barely shows any shift with changing cooling rate. This shows up as a tilt of the top of the error function relative to the bottom.
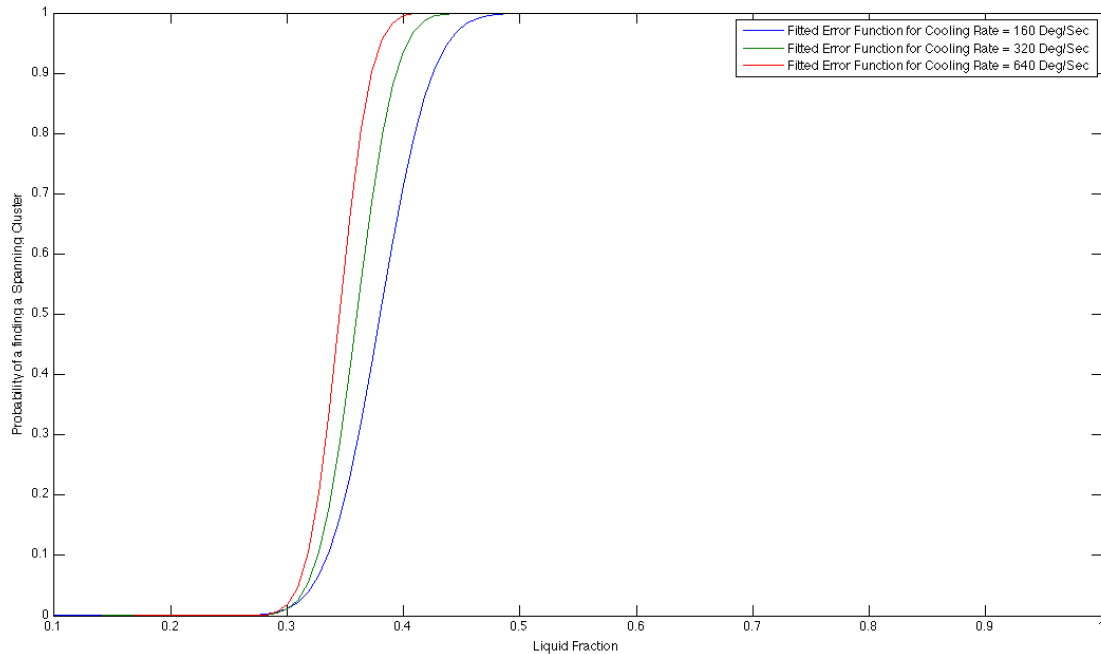

Figure 35 - Probability of having a Spanning Cluster vs. Liquid Fraction for varying cooling rates fitted to equation 44 using parameters given in Table 1

5.4–ANALYSIS OF SIZE DISTRIBUTIONS OF LIQUID POOLS

Clustering analysis can also highlight the size distributions of evolving liquid pools. Normalized averaged size distributions for the cases of varying cooling rates and diffusion coefficients are discussed in the following sub-sections. For both cases the size distributions are very rough, even after averaging over ten trials. However, they do exhibit trends that explain liquid pool evolution further. Each set of size distributions shown correspond to the onset of coarsening, the onset coalescence, and when both coarsening and coalescence processes are active. Snapshots of simulated microstructure are also shown alongside.

5.4.1 – SIZE DISTRIBUTIONS FOR VARYING SOLIDDIFFUSION COEFFICIENTS

For the case of varying diffusion coefficients, the normalized size distributions are shown in Figure 36 through Figure 39. They roughly overlay each other, implying little variance in structure. This can also be linked back to the error fits, which showed a minimal variation. Two small peaks can also be observed, with the larger one occurring at smaller normalized size. The large and small peaks speak to the number and sizes of liquid pool networks and isolated pools respectively. As coalescence processes start operating, the liquid pool networks are pinched off to form isolated pools, leading to disappearance of two distinct peaks.

Figure 36 - Size distributions of Liquid Pools with varying solid diffusion coefficients corresponding to the onset of coarsening. The second and third thumbnails show progressively magnified views, also indicated by the scales on the y-axis
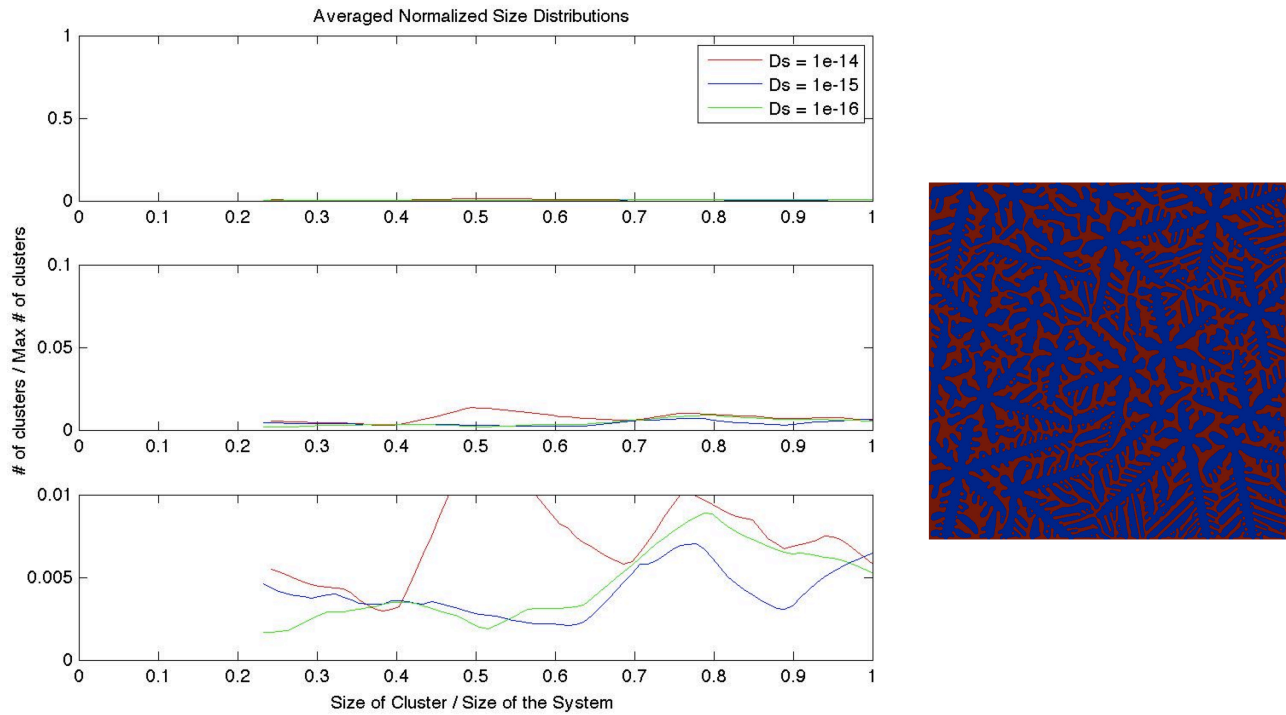
Figure 37 - Size distributions of Liquid Pools with varying solid diffusion coefficients corresponding to the onset of coalescence. The second and third thumbnails show progressively magnified views, also indicated by the scales on the y-axis

Figure 38 -Size distributions of Liquid Pools with varying solid diffusion coefficients corresponding to the when both coarsening and coalescence processes are active. The second and third thumbnails show progressively magnified views, also indicated by the scales on the y-axis

5.4.2 – SIZE DISTRIBUTIONS FOR VARYING COOLING RATES

Figure 39 through Figure 41 show size distributions for the case of varying cooling rates. In this case it is difficult to draw out a noticeable trend. An expected result would be to get distributions that roughly overlay each other as in the varying diffusion coefficients case, with the two peaks being taller and sharper for higher cooling rates. This would be consistent with visual inspection where the sharper peaks imply less available room/sizes at higher cooling rates/grain densities. The taller peaks would imply a larger number of liquid pools at these smaller sizes. As in the previous case, the normalized number times size would then be an indication of the amount (in liquid fraction) of such liquid pools.

Additionally, the universality argument presented in (Aagesen et al., 2010) can be brought into focus, where the interface morphologies were shown to be universal across solidifying systems. Accordingly, a lower cooling rate produces microstructure that, at the same non-equilibrium temperature, resembles that of a higher cooling rate at magnification. The chaotic appearance and evolution of liquid pools therefore has a universal semblance. This is evidenced in the normalized size distributions, where they overlay each other with varying cooling rates. Here it is hypothesized that the number of liquid pools as determined by the Hoshen-Kopleman clustering algorithm may be some scalable number where:

$$\left(Size\right)_{NORMALIZED}\left(Number\right)_{NORMALIZED}^{scalable}=\left(Size\right)_{REAL} \qquad \textbf{Eq. 45}$$

Regardless, any interpretation with the size distributions presented for the case of varying cooling rates is speculation. A larger data set that provides further statistics is needed to test this speculation.

Figure 39 -- Size distributions of Liquid Pools with varying cooling rates corresponding to the onset of coarsening. The second and third thumbnails show progressively magnified views, also indicated by the scales on the y-axis
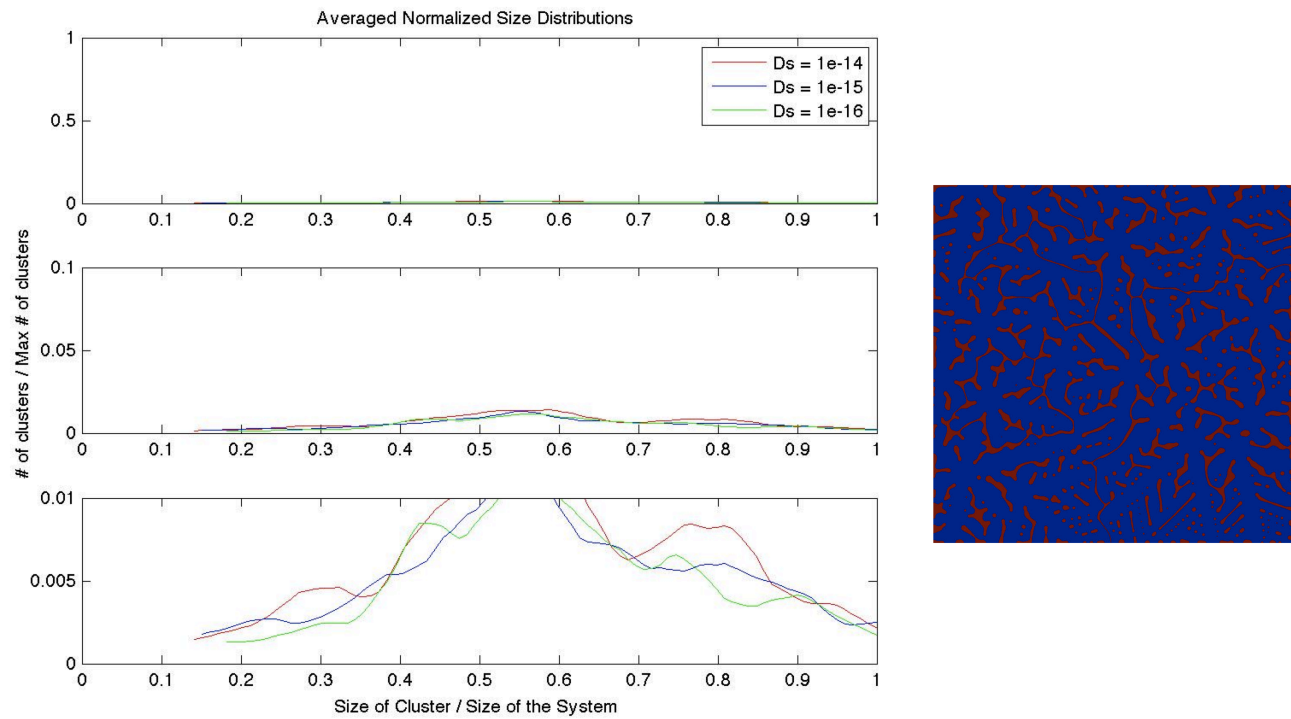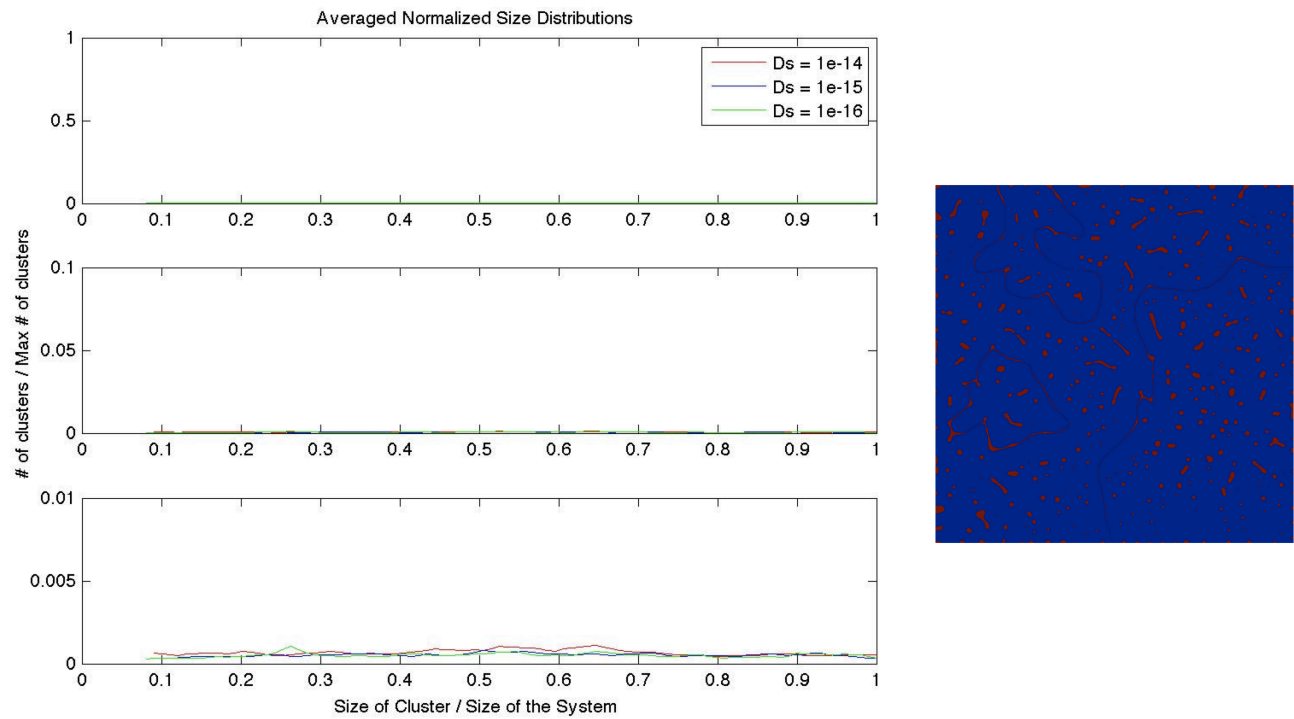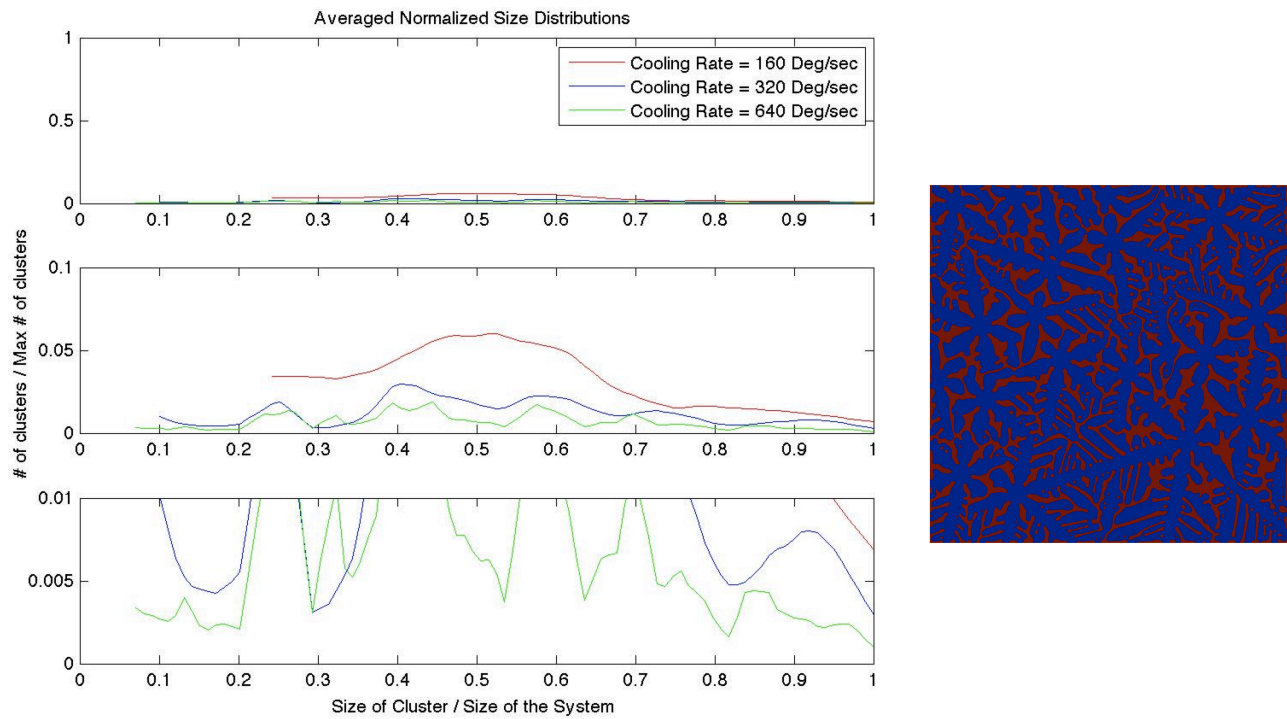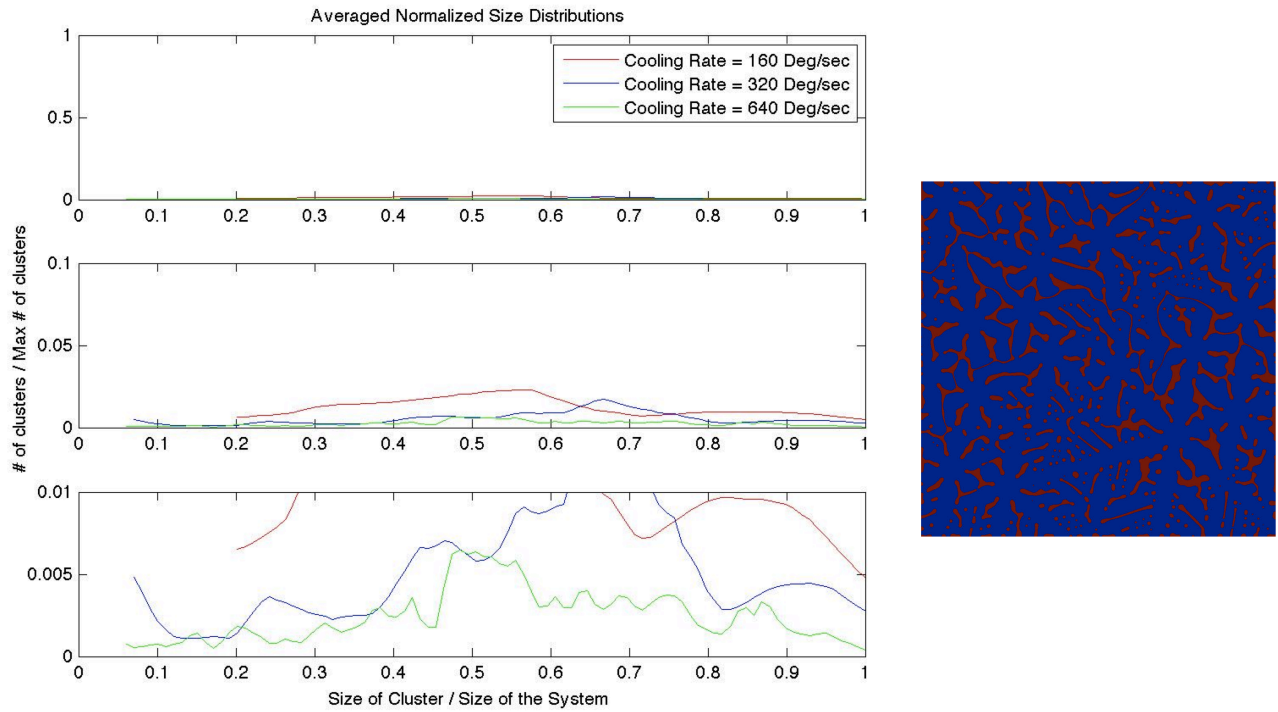
Figure 40 -Size distributions of Liquid Pools with varying cooling rates corresponding to the onset of coalescence. The second and third thumbnails show progressively magnified views, also indicated by the scales on the y-axis
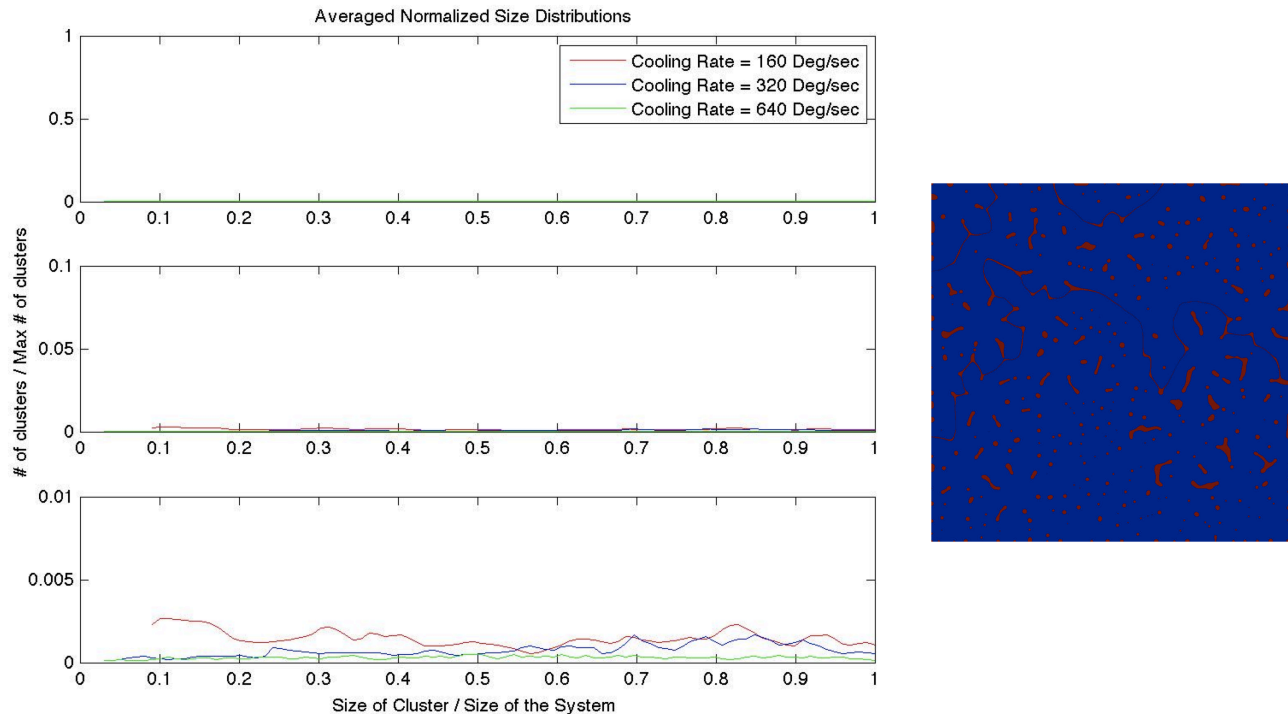
Figure 41 - Size distributions of Liquid Pools with varying solid diffusion coefficients corresponding to the when both coarsening and coalescence processes are active. The second and third thumbnails show progressively magnified views, also indicated by the scales on the y-axis

5.4.3 – COMMENTS ON RESULTS OF CLUSTERING ALGORITHM

Finally, with regards to second phase formation the clustering analysis presented above and any associated percolation methods can be truly useful when coupled with a thermodynamic analysis that tracks the liquid pool compositions and actively computes nucleation driving forces for second phases. The liquid pool networks that are true precursors for second phases can then be identified, along with their numbers, sizes and spatial distributions.

Improvements can also be made to the Hoshen-Kopleman algorithm, which would only serve to make it more robust and accurate. Notably, the algorithm sometimes does not recognize large connected pools. An example is given in Figure 42 where the white circles highlight

connected pools identified as separate ones. It is assumed that for the purposes of this study that the algorithm performs adequately, and averaging over many trials reduces any prevailing errors.
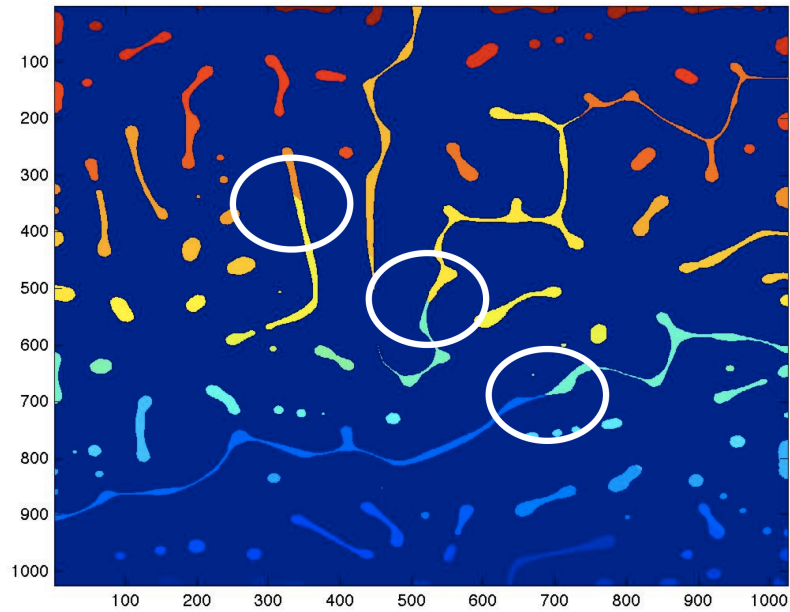

Figure 42 – Example of the Hoshen-Kopleman algorithm's misbehavior

CHAPTER 6 – CONCLUSIONS

In this thesis, late stage liquid pools were identified as an important morphological feature in the context of second phase formation and spatial distribution. Some studies were highlighted that focused on second phase selection and spatial distribution, along with some novel techniques and methods to analyze microstructural features. These included spectral, clustering and percolation analysis and subsequently were used to analyze simulated microstructure produced using a phase field model.

Spectral and clustering analyses were shown to be complementary tools that each gives insight into liquid pool evolution in unique ways. Spectral analysis showed that self-affine scaling exists through some lengthscales of liquid pools, while clustering analysis was crucial in isolating liquid pools from among other features present in solidifying microstructures. Liquid Pool evolution was shown to exhibit a general trend, and variations in this trend were investigated with changing cooling rates and solid diffusion coefficient.

The general trend shown by liquid pool evolution exhibits five regimes that tell of different processes active at various points in the solidification process. In the context of second phase formation, the coarsening regime is hypothesized to be the most important since it precedes coalescence processes that take away solute which may be required for initial second phase formation. Percolation analysis applied to clustering analysis results allowed for the changes in the coarsening regime to be quantified. Specifically, it was found that the onset of coarsening occurs at lower liquid fractions at higher cooling rates, leading to large number of small sized liquid pools. It was also found that higher solid diffusion coefficients (analogous to back diffusion) show more rapid coalescence processes, which also would lead to smaller sized liquid pools. However, this effect with varying solid diffusion rates was small.

Additionally, size distribution analysis of liquid pool evolution was also performed, which at best allowed for speculation. It is hypothesized that the number of clusters across various cooling rates may be a scalable quantity, and as such implies extrapolation of results for

other solidification conditions. Investigating the limits of such an extrapolation in the context of industrial use is an absolute must. For such an analysis, there is a need for better statistics (and computational resources). Furthermore, a temperature dependant solid diffusion coefficient is a realistic feature for all solidifying systems, and corresponding results can be expected to be a mixture of the ones from varying cooling rates and solid diffusion coefficients.

With regards to the long term goal of obtaining a theory that correlates liquid pool evolution with second phase formation, a thermodynamic analysis that couples with the ones presented in this thesis is crucial. It will particularly be useful for the study solidification of ternary systems, where multiple possible second phases will allow corresponding liquid pools (precursors) to be identified and spatial distributions unique to *different* second phases to be analyzed.

BIBLIOGRAPHY

Aagesen, L. K., Johnson, A. E., Fife, J. L., Voorhees, P. W., Miksis, M. J., Poulsen, S. O., Lauridsen, E. M., et al. (2010). Universality and self-similarity in pinch-off of rods by bulk diffusion, *6*(October), 2–6. doi:10.1038/NPHYS1737

Amoorezaei, M. (2012). *Near-surface Microstructure of Cast Aluminum and Magnesium Alloys*. McMaster University.

Amoorezaei, M., Gurevich, S., & Provatas, N. (2010). Spacing characterization in Al–Cu alloys directionally solidified under transient growth conditions. *Acta Materialia*, *58*(18), 6115–6124. doi:10.1016/j.actamat.2010.07.029

Amoorezaei, M., Gurevich, S., & Provatas, N. (2012). Orientation selection in solidification patterning. *Acta Materialia*, *60*(2), 657–663. doi:10.1016/j.actamat.2011.10.006

Brunini, V., Schuh, C., & Carter, W. (2011). Percolation of diffusionally evolved two-phase systems. *Physical Review E*, *83*(2), 1–9. doi:10.1103/PhysRevE.83.021119

Cahn, J. (1962). The impurity-Drag Effect in Grain Boundary Motion. *Acta metallurgica*, , 10, 9, 1962, 789-798

Cahn, J. W., & Hilliard, J. E. (1958). Free Energy of a Nonuniform System. I. Interfacial Free Energy. *The Journal of Chemical Physics*, *28*(2), 258. doi:10.1063/1.1744102

Cahn, J. W., & Hilliard, J. E. (1959). Free Energy of a Nonuniform System. III. Nucleation in a Two-Component Incompressible Fluid. *The Journal of Chemical Physics*, *31*(3), 688. doi:10.1063/1.1730447

Czerwinski, F. (Ed.). (2011). *Magnesium Alloys - Design, Processing and Properties* (p. 526). InTech. doi:10.5772/560

Dahle, A., Lee, Y., & Nave, M. (2001). Development of the as-cast microstructure in magnesium-aluminium alloys. *Journal of light metals*, *1*, 61–72.

Dantzig, J. ., & Rappaz, M. (2009). *Solidification* (p. 618). Boca Ranton: EPFL Press.

Ekström, H. E., Hagström, J., & Östensson, L. (2000). Particle Size Distributions in a DC-Cast and Rolled AA3104 Alloy. *Materials Science Forum*, *331-337*, 179–184.

Fisher, K., & Kurz, W. (1998). *Fundamentals of solidification* (p. 305). Enfield: Enfield Publishing & Distribution Company.

Fricke, T. (2004). The Hoshen-Kopelman Algorithm.

Glicksman, M. E., Smith, R. N., Marsh, S. P., & Kuklinski, R. (1992). Mushy Zone Modeling with Microstructural Coarsening Kinetics, *23*(February).

Greenwood, M. (2004). *Scaling in directional solidification of binary alloys*. McMaster University.

Grey, E., & Higgins, G. (1973). Solute Limited Grain Boundary Migration: A Rationalisation of Grain Growth. *Acta Metallurgica*, *21*(April).

Gupta, A., Marois, P., & Lloyd, D. (1996). Review of the techniques for the extraction of second-phase particles from aluminum alloys. *Materials characterization*, *445803*(96).

Gurevich, S., Amoorezaei, M., Montiel, D., & Provatas, N. (2012). Evolution of microstructural length scales during solidification of magnesium alloys. *Acta Materialia*, *60*(8), 3287–3295. doi:10.1016/j.actamat.2012.02.055

Gurevich, S., Amoorezaei, M., & Provatas, N. (2010). Phase-field study of spacing evolution during transient growth. *Physical Review E*, *82*(5), 1–8. doi:10.1103/PhysRevE.82.051606

Heinz, a, Haszler, a, Keidel, C., Moldenhauer, S., Benedictus, R., & Miller, W. . (2000). Recent development in aluminium alloys for aerospace applications. *Materials Science and Engineering: A*, *280*(1), 102–107. doi:10.1016/S0921-5093(99)00674-7

Hohenberg, P., & Halperin, B. (1977). Theory of dynamic critical phenomena. *Reviews of Modern Physics*, (3).

Kailasam, S. K., Glicksman, M. E., Mani, S. S., & Fradkov, V. E. (1999). Investigation of Microstructural Coarsening in Sn-Pb Alloys, *30*(June), 1541–1547.

Khajeh, E., & Maijer, D. M. (2010). Inverse Analysis of Eutectic Nucleation and Growth Kinetics in Hypoeutectic Al-Cu Alloys. *Metallurgical and Materials Transactions A*, *42*(1), 158–169. doi:10.1007/s11661-010-0489-7

Lifshitz, I., & Slyozov, V. (1961). The kinetics of precipitation from supersaturated solid solutions. *Journal of Physics and Chemistry of Solids*, *19*(1), 35–50.

Lu, J., Wiskel, J. B., Omotoso, O., Henein, H., & Ivey, D. G. (2010). Matrix Dissolution Techniques Applied to Extract and Quantify Precipitates from a Microalloyed Steel. *Metallurgical and Materials Transactions A*, *42*(7), 1767–1784. doi:10.1007/s11661-010-0579-6

Malakhov, D. V., Panahi, D., & Gallerneault, M. (2010). On the formation of intermetallics in rapidly solidifying Al–Fe–Si alloys. *Calphad*, *34*(2), 159–166. doi:10.1016/j.calphad.2010.01.006

Mikhaylovskaya, a. V., Ryazantseva, M. a., & Portnoy, V. K. (2011). Effect of eutectic particles on the grain size control and the superplasticity of aluminium alloys. *Materials Science and Engineering: A*, *528*(24), 7306–7309. doi:10.1016/j.msea.2011.06.042

Mortensen, A. (1989). On the Influence of Coarsening on Microsegregation, *20*(February), 247–253.

Ofori-Opoku, N., & Provatas, N. (2010). A quantitative multi-phase field model of polycrystalline alloy solidification. *Acta Materialia*, *58*(6), 2155–2164. doi:10.1016/j.actamat.2009.12.001

Oldfield, W. (1966). A QUANTITATIVE APPROACH TO CASTING SOLIDIFICATION--FREEZING OF CAST IRON. *ASM Trans Quart*.

Prasad, A., Henein, H., Maire, E., & Gandin, C. (2006). Understanding the Rapid Solidification of Al-4 . 3Cu and Al-17Cu Using X-Ray Tomography, *37*(JANUARY).

Quested, T. ., & Greer, a. . (2004). The effect of the size distribution of inoculant particles on as-cast grain size in aluminium alloys. *Acta Materialia*, *52*(13), 3859–3868. doi:10.1016/j.actamat.2004.04.035

Rappaz, M., Jacot, A., & Boettinger, W. (2003). Last-stage solidification of alloys: Theoretical model of dendrite-arm and grain coalescence. *Metallurgical and Materials …*, *34*(March).

Rowlinson, J. (1979). Translation of J . D . van der Waals ' " The Thermodynamic Theory of Capillarity Under the Hypothesis of a Continuous Variation of Density . *Journal of Statistical Physics*, *20*(2), 1975–1978.

Sarreal, J. A., & Abbaschian, G. J. (1986). The Effect of Solidification Rate on Microsegregation, *17*(NOVEMBER), 2063–2073.

Simmons, J. ., Shen, C., & Wang, Y. (2000). Phase field modeling of simultaneous nucleation and growth by explicitly incorporating nucleation events. *Scripta Materialia*, *43*(10), 935–942. doi:10.1016/S1359-6462(00)00517-0

Starke, E., & Staley, J. (1996). Application of Modern Aluminum Alloys to Aircraft. *Progress in Aerospace Sciences*, *32*(95), 131–172.

Volmer, M., & Weber, A. (1926). Keimbildung in Übersättigten Gebilden. *Z. phys. Chem*.

Zeldovich, Y. (1943). On the theory of new phase formation, cavitation. *Acta Physicochim. URSS*.